Highlights

Lunar gravitational maps from GRAIL gravity, LRO and Kaguya topography and 3D crustal density

Blažej Bucha

- Lunar gravitational maps are derived from satellite and topography-induced gravity
- The maps show the gravitational potential, vector and tensor at the 250-m resolution
- 3D variable density is used to compute topography-induced gravitational signals
- Gravitational field is expanded up to degree 11,519 in terms of spherical harmonics
- The maps are suitable for engineering applications such as navigation

Lunar gravitational maps from GRAIL gravity, LRO and Kaguya topography and 3D crustal density

Blažej Bucha[a]

[a]Department of Theoretical Geodesy and Geoinformatics, Slovak University of Technology in Bratislava, Radlinského 11, Bratislava 81005, Slovak Republic

ARTICLE INFO

Keywords:
Lunar gravitational field
Satellite gravity
Topography
3D variable density
Gravity-forward modeling

ABSTRACT

We present a suite of Lunar Gravitational Maps 2026 (LGM2026) at a resolution of 128 pixels per degree (∼250 m at the equator). The maps show the gravitational potential, the gravitational vector and the gravitational tensor globally at the lunar surface and on its circumscribing sphere. Long wavelengths up to 11 km are taken from a spherical-harmonic model derived from the Gravity Recovery and Interior Laboratory mission (GRAIL). The remaining short wavelengths are forward-modeled from the lunar topography observed by the Lunar Reconnaissance Orbiter (LRO) and the Kaguya spacecraft using a 3D crustal density model. Over most regions, the commission error of LGM2026 is estimated at 2 mGal for the gravitational vector. LGM2026 can be beneficial for near-surface applications that are sensitive to variations of the lunar gravitational field such as spacecraft navigation, inertial navigation or gravity field simulations. Given that the gravitational signals beyond the 11-km resolution are modeled from topography, they cannot, however, be geophysically or geologically interpreted. As a by-product, LGM2026 was converted into an external solid spherical-harmonic expansion of the gravitational potential up to degree 11,519.

1. Introduction

Knowledge of the lunar gravity field is essential to understand the interior structure of the Moon (Wieczorek et al., 2013), for topography mapping (Barker et al., 2016) or for spacecraft navigation (Chen et al., 2023). A breakthrough in lunar gravity field mapping was achieved by the Gravity Recovery and Interior Laboratory mission (GRAIL; Zuber et al., 2013). The GRAIL satellites were, however, insensitive to gravity features beyond the resolution of a few kilometers (Wieczorek, 2015). Such fine-scale gravity signals are essential, for instance, for spacecraft navigation at landing sites as demonstrated by the Mars rover Curiosity (Way, 2013). In the context of the lunar gravity field, these short wavelengths originate almost exclusively from topography and subsurface mass variations (Zuber et al., 2013; Goossens et al., 2020). Therefore, they can be predicted from the shape and density of topography by means of Newton's law of gravitation.

Thanks to the Lunar Reconnaissance Orbiter (LRO; Chin et al., 2007) and the Kaguya missions (Kato et al., 2010), lunar topography models have reached resolutions of a few tens of meters globally (Barker et al., 2016). They are thus better resolved than GRAIL gravity models by two orders of magnitude, making them suitable for short-scale gravity predictions. Supplementing observed gravity with gravity from topography is a well-established methodology (Tziavos and Sideris, 2013), which, under some variations, has been applied to the Earth (Pavlis et al., 2012; Hirt et al., 2013; Ince et al., 2020), the Moon (Hirt and Featherstone, 2012), Mars (Hirt et al., 2012; Górski et al., 2018) or Venus (Li et al., 2015). By incorporating topography-implied signals, these models may describe gravity fields more accurately and completely than those relying solely on gravity observations (e.g., Hirt et al., 2013), although they can no longer be used in geological and geophysical applications. Presently, the most detailed lunar surface gravity model employing gravity predictions from topography is the Lunar Gravity Model 2011 (LGM2011) with its 1.5-km resolution at the equator (Hirt and Featherstone, 2012). However, more than a decade after its release, the data and methodology behind LGM2011 no longer represent the state of the art. First, new LRO topography data were gathered which led to improved lunar shape models (Barker et al., 2016). Second, the topography-induced gravity in LGM2011 assumes constant-density topography, but lateral and 3D density modeling have been studied increasingly (Wieczorek et al., 2013; Besserer et al., 2014; Han et al., 2014; Goossens et al., 2020; Šprlák et al., 2020). Third, on the methodological level, the topography-based component of LGM2011 employs the outdated planar approximation and does not incorporate certain correction terms that were later discovered by Rexer et al. (2018). These recent developments stimulate a compilation of new lunar gravitational maps for the benefit of future scientific and engineering applications.

Taking advantage of the new datasets (Section 2) and modeling techniques (Section 3), we developed a suit of Lunar Gravitational Maps 2026 (LGM2026; Section 4) that surpass previous efforts in several aspects. The maps show not only the gravitational potential and vector as in LGM2011, but also the gravitational tensor. Each quantity is modeled globally at the lunar surface and on its circumscribing sphere. The resolution of LGM2026 is 128 pixels per degree (PPD), which corresponds to about ∼250 m at the equator, outperforming LGM2011 by a factor of ∼6. In terms of data, LGM2026 benefits from latests state-of-the-art models of gravity from GRAIL, topography from LRO and Kaguya, and 3D crustal density from inversion of GRAIL data. Finally, given that 3D crustal density models yield superior

blazej.bucha@stuba.sk (B. Bucha)
ORCID(s): 0009-0006-1694-1544 (B. Bucha)

topography-implied gravity compared to constant-density models (Šprlák et al., 2018; Bucha, 2025), LGM2026's shift to 3D densities represents a step towards more realistic short-scale gravity predictions. The commission error of LGM2026 is estimated at 2 mGal for the gravitational vector at the lunar surface (1 mGal = 10^{-5} m s^{-2}; Section 5). LGM2026 can be suitable for gravity predictions at prospective landing sites, spacecraft navigation and other applications seeking fine-scale surface gravitational information (Section 6). As the primary limitation, LGM2026 is not suitable for geophysical and geological interpretations at scales smaller than 11 km at the equator (Section 7).

2. Data

Long wavelengths of LGM2026 were taken from the Kaula-constrained spherical-harmonic model GRGM1200B (Goossens et al., 2020) up to degree 500 (∼11 km at the equator). GRGM1200B relies on the primary and extended mission GRAIL data and is expanded up to degree 1200.

In short wavelengths beyond degree 500, LGM2026 relies on gravity inferred from topography and density models. The topography was represented by the LDEM128_PA_pixel_202405 model (briefly LDEM128; Neumann, 2024) at the resolution of 128 PPD. LDEM128 is based on data from the Lunar Orbiter Laser Altimeter (LOLA) onboard LRO and from the Kaguya's Terrain Camera. It is expressed in the Moon's principal axes coordinate system (PA), matching the coordinate system of GRGM1200B. For the spherical-harmonic representation of LDEM128, we used the degree-11,519 model Moon_LDEM128_shape_pa_11519 (briefly LDEM128_SH; Wieczorek, 2024). The density was represented by the linear 3D model of Goossens et al. (2020) using the variant with the cap radius of 15° and the degree range 250–650.

3. Methods

LGM2026 builds on principles established over four decades of Earth's gravity field modeling. The key idea is to (i) base the gravity model on gravity observations whenever possible and (ii) employ gravity predictions from topography once the observations are too noisy or unavailable in some regions. Owing to the strong correlation between topography and the gravity field of planets at short scales, this approach can approximate even the finest gravity structures, making it useful for applications ranging from geoid determination (e.g., Sansò and Sideris, 2013) to spacecraft navigation (e.g., Górski et al., 2018). As a limitation, those parts of the model that incorporate gravity predictions from topography, be it in the spectral or spatial domain, cannot be geologically or geophysically interpreted, which rules out applications such as gravity inversions.

LGM2026 takes long-wavelength gravity from GRAIL satellites (wavelengths up to 11 km at the equator) and combines it with fine gravity signals implied by near-surface lunar topographic masses (wavelengths shorter than 11 km). Unique to LGM2026 is its approach to gravity predictions, which exploit 3D variable crustal density information.

Given the fine target resolution of 250 m and our focus on the gravitational field at the lunar surface, LGM2026 cannot be parametrized by the popular external spherical harmonics, as the series diverges at the lunar surface at even coarser resolutions, say, a few kilometers (e.g., Hirt and Kuhn, 2017; Šprlák and Han, 2021). We therefore rely on the parametrization by 2D grids, which can be regarded as maps (for other approaches, see, e.g., Takahashi and Scheeres 2014 or Grafarend and Engels 1993). LGM2026 maps show the gravitational potential V, the gravitational vector

$$\vec{g} = \nabla V = \begin{bmatrix} V^{\mathrm{x}} \\ V^{\mathrm{y}} \\ V^{\mathrm{z}} \end{bmatrix} \tag{1}$$

and the gravitational tensor

$$\mathbf{V} = \nabla \otimes \nabla V = \begin{bmatrix} V^{\mathrm{xx}} & V^{\mathrm{xy}} & V^{\mathrm{xz}} \\ V^{\mathrm{yx}} & V^{\mathrm{yy}} & V^{\mathrm{yz}} \\ V^{\mathrm{zx}} & V^{\mathrm{zy}} & V^{\mathrm{zz}} \end{bmatrix}. \tag{2}$$

The gravitational vector and tensor are expressed in the local north-oriented reference frame (LNOF), which is a right-handed Cartesian coordinate system with the origin at the evaluation point, the x-axis pointing to the north, the y-axis pointing to the west and the z-axis pointing radially outwards. All quantities are provided 0.1 m above the lunar topography as represented by LDEM128 (hereafter referred to as *at the topography* for brevity) and on the sphere of the radius 1749 km passing outside lunar masses (*on the circumscribing sphere* for brevity). Neither the centrifugal field nor the normal gravity field is included in LGM2026. Given that the 3D position of the LGM2026 points is published along with the maps, they can readily be evaluated whenever necessary.

All LGM2026 quantities, V, $\vec{g}$ and $\mathbf{V}$, were computed in the same manner, so we shall demonstrate the development strategy using the gravitational potential V only. The gravitational potential V was obtained as

$$V = V^{\mathrm{GGM}} + V^{\mathrm{RTM}}, \tag{3}$$

where V^{GGM} is the long-wavelength component from the global gravity model GRGM1200B (Section 3.1) and V^{RTM} is the short-wavelength signal beyond degree 500 predicted from topography using residual terrain modeling (RTM; Section 3.2). To ensure that V^{RTM} does not interfere with V^{GGM}, RTM corrections introduced by Rexer et al. (2018) are taken into account in V^{RTM} (Sections 3.2.1 and 3.2.2).

3.1. Long-wavelength component

The long wavelength component V^{GGM} from Eq. (3) relies on observed GRAIL gravitational data through the Kaula-constrained GRGM1200B model (briefly GRGM1200B). The term was obtained by the solid spherical-harmonic synthesis of the $\bar{V}_{nm}^{\mathrm{GGM}}$ coefficients from GRGM1200B up to degree 500 using the relation

$$V^{\mathrm{GGM}}(r,\varphi,\lambda) = \frac{\mathrm{GM}^{\mathrm{GGM}}}{R^{\mathrm{GGM}}} \sum_{n=0}^{500} \left(\frac{R^{\mathrm{GGM}}}{r}\right)^{n+1} \times \sum_{m=-n}^{n} \bar{V}_{nm}^{\mathrm{GGM}}\, \bar{Y}_{nm}(\varphi,\lambda), \tag{4}$$

where r, φ, λ are the spherical radius, the spherical latitude and the spherical longitude of evaluation points, $\mathrm{GM}^{\mathrm{GGM}}$ is the product of Newton's gravitational constant and mass of the Moon, R^{GGM} is the radius of the reference lunar sphere and $\bar{Y}_{nm}(\varphi,\lambda)$ are the 4π-fully normalized surface spherical harmonics of degree n and order m. The scaling constants $\mathrm{GM}^{\mathrm{GGM}}$ and R^{GGM} are given by GRGM1200B. Since GRGM1200B does not specify the coefficient $\bar{V}_{00}^{\mathrm{GGM}}$ of degree and order 0, we set it to 1, so that the dominant monopole component reads $\mathrm{GM}^{\mathrm{GGM}}/r$.

We truncated the series (4) at degree 500, because neither too low nor too high truncation degree is a good choice for LGM2026. If truncated too early, the series will not capture valuable gravitational signals observed by GRAIL. If the series is truncated too late, the following points should be considered.

1. The constraints that were used to estimate GRGM1200B will propagate into the gravitational quantities. For the GRGM1200B variant that we used, the constraint is the Kaula rule, which is an empirical power law. This rule, however, seems to be too strong (Šprlák and Han, 2021) and thus it may smooth GRAIL observations, leaving un-modeled signals in high degrees. Fig. 5a of Goossens et al. (2020) shows that the model remains mostly unaffected by the Kaula regularization up to degree 500 (Kaula constraint applied beyond degree 600). Alternatively, the RM1 variants of GRGM1200B (see Goossens et al., 2020) could be used that employ a regularization based on topography-implied gravity instead of the Kaula rule. But in principle, this is the same as what our RTM method does, although our RTM does not take advantage of GRAIL observations beyond degree 500 as it happens with GRGM1200B + RM1.
2. The series will be subject to the divergence of spherical harmonics at the lunar topography. It has been shown numerically that the potential series evaluated at the lunar surface starts to deviate from the true potential somewhere around degree 700 due to the series divergence (Hirt and Kuhn, 2017). This is in agreement with the theory, which guarantees convergence outside the smallest lunar circumscribing sphere only (Sansò, 2013). Rigorously speaking, one should therefore reject the idea of evaluating the series at the lunar surface, regardless of the truncation degree. Another option is to be aware of the divergence and to try to determine the turning point, beyond which partial sums of the series start to deviate from the true value, hoping the bottom part of the series can realistically model the true signal. Such an analysis has been done by Hirt and Kuhn (2017) and the turning point seems to be somewhere around degree 700.
3. High-frequency noise in GRAIL data will be amplified disproportionally when the series is evaluated at the topography due to the downward continuation.
4. Degree strengths will spatially vary, making the model less homogeneous.

By relying on the Kaula-constrained GRGM1200B truncated at degree 500, we thus (i) mitigate the impact of regularization methods (the unconstrained GRGM1200B is not publicly available), (ii) mitigate the divergence of spherical harmonics at the lunar surface, (iii) avoid too strong noise amplification and (iv) ensure spatially homogeneous degree strengths.

Given the low truncation degree of 500, we used the exact algorithm for solid synthesis both at the lunar surface and on its circumscribing sphere, avoiding the more efficient but approximate gradient approach (e.g., Balmino et al., 2012; Hirt, 2012). To this end, we used CHarm, a C/Python library for spherical-harmonic transforms in planetary geodesy (Bucha, 2026). The evaluation of Eq. (4) was parallelized using OpenMP and AVX2.

3.2. Short-wavelength component

The short-wavelength signals V^{RTM} from Eq. (3) were delivered by RTM (Forsberg and Tscherning, 1981; Torge and Müller, 2012; Tziavos and Sideris, 2013). This component does not rely on any observed gravitational data but instead approximates the gravitational field based on the lunar topography and its density. To make the modeling closer to the reality, we employed a 3D crustal density model as opposed to the previously used constant density model (Hirt and Featherstone, 2012). Our RTM modeling assumes isostatically uncompensated lunar topography beyond degree 500, that is, at wavelengths shorter than $\sim$11 km at the equator. These fine topographic features are thus assumed to be not supported by deeper mass adjustments in the crust or upper mantle which is a realistic assumption (Wieczorek et al., 2013).

In principle, RTM first forms a residual terrain by subtracting long-wavelength topography (here LDEM128_SH to degree 500) from high-resolution topography (here LDEM128). Then, it calculates gravitational effects of the residual terrain using Newton's integral. Because the short-scale residual terrain is isostatically uncompensated, the integration can be limited to nearby masses (typically within a few tens of kilometers of evaluation points), improving efficiency over global integration. Finally, the gravitational effects are adjusted for low- and high-frequency corrections (Rexer et al., 2018) to make RTM signals consistent with spherical-harmonic gravitational models that are expanded up to the same degree as the long-wavelength topography (here GRGM1200B to degree 500). By adding short-scale topography-implied RTM signals (V^{RTM} in Eq. 3) to long-wavelength observed gravity from spherical-harmonic models (V^{GGM} in Eq. 3), the completeness and resolution of the latter may be substantially improved. Numerous Earth-related studies proved indeed that RTM reduces the omission error of spherical-harmonic gravity models, in some cases by as much as 80 % (Hirt et al., 2013; Ďuríčková and Janák, 2016; Grombein et al., 2017). Improvements were also observed with lunar (Hirt and Featherstone, 2012) and martian gravity fields (Hirt et al., 2012; Way, 2013), though with less confidence due to the lack of surface gravity observations (at the lunar surface, only a few gravity observations from the Apollo era are available).

RTM can be viewed as high-pass filtering of gravitational fields implied by high-resolution topographies. For proper filtering, it is crucial to ensure consistency between the high-resolution and long-wavelength topographies (Hirt et al., 2014). In our case, the consistency is guaranteed, as LDEM128_SH was obtained directly from LDEM128 by spherical-harmonic analysis (Wieczorek, 2024).

Let us assume that LDEM128 (the high-resolution topography) and LDEM128_SH (the long-wavelength topography) were referenced to an internal sphere of the radius 1727 km, so that all heights are positive. Furthermore, let us formally denote by $\mathcal{G}(\text{DEM})$ the process of evaluating some functional of the gravitational potential implied by a digital elevation model DEM. This process is often called gravity-forward modeling or gravity-from-topography modeling. Then, RTM modeling reads

$$\begin{aligned} V^{\text{RTM}} = {} & \mathcal{G}^{T,\psi<180^\circ}_{0..\infty}(\text{LDEM128}_{0..\infty}) \\ & - \mathcal{G}^{\text{SH},\psi<180^\circ}_{0..500}(\text{LDEM128\_SH}_{0..500}) - \text{LF}. \end{aligned} \tag{5}$$

Here, the subscripts indicate the spectral content. For instance, $\text{LDEM128\_SH}_{0..500}$ means that LDEM128_SH is expanded from degree 0 up to degree 500, $\mathcal{G}_{0..500}$ means that the gravitational effects from gravity-forward modeling are considered from degree 0 to 500 and so on. The first superscript next to $\mathcal{G}$ denotes gravity-forward modeling method: $\mathcal{G}^T$ stands for a spatial-domain method (Section 3.3.1) and $\mathcal{G}^{\text{SH}}$ denotes a spherical-harmonic method (Section 3.3.2). The second superscript next to $\mathcal{G}$ uses the spherical distance ψ between the evaluation point and topographic masses to indicate masses that are gravity-forward modeled: $\psi < 180^\circ$ therefore implies integration of all masses (global integration). Finally, LF stands for the low-frequency correction.

The rationale behind Eq. (5) is as follows. The first term on the right-hand side, $\mathcal{G}^{T,\psi<180^\circ}_{0..\infty}(\text{LDEM128}_{0..\infty})$, represents the full-spectrum gravitational field of the high-resolution full-spectrum topography LDEM128. It contains gravity signals not only beyond degree 500, as required to augment GRGM1200B truncated at degree 500 (see Eqs. 3 and 4), but also signals at degrees 0 to 500. To be able to use it in conjunction with GRGM1200B, all signal power at degrees from 0 to 500 must therefore be removed. We achieve this in two steps. First, we subtract $\mathcal{G}^{\text{SH},\psi<180^\circ}_{0..500}(\text{LDEM128\_SH}_{0..500})$, which stands for the gravitational field of LDEM128_SH, where both the gravitational field and LDEM128_SH are expanded to degree 500. After the subtraction, a significant portion of the signals in $\mathcal{G}^{T,\psi<180^\circ}_{0..\infty}(\text{LDEM128}_{0..\infty})$ is removed at degrees 0 to 500, while degrees beyond 500 remain untouched, because the gravity signals $\mathcal{G}^{\text{SH},\psi<180^\circ}_{0..500}(\text{LDEM128\_SH}_{0..500})$ are truncated at degree 500. However, some leftover signals can still be found in harmonics up to degree 500, given that LDEM128_SH was truncated at degree 500 instead of being expanded up to infinity to match the other term (see Eq. 5). In the second step, we thus remove the leftover signals, so that RTM indeed covers only harmonics beyond degree 500 as required by Eq. (3). This is done by subtracting the LF correction term, which represents errors committed by using $\text{LDEM128\_SH}_{0..500}$ in the second term on the right-hand side of Eq. (5) instead of using LDEM128. Evaluation of this correction will be discussed later in Section 3.2.2.

Global spatial-domain gravity-forward modeling $\mathcal{G}^{T,\psi<180^\circ}_{0..\infty}$ from Eq. (5) is computationally challenging due to the convolutional character of Newton's integral. Opposed to this, spectral spherical-harmonic methods $\mathcal{G}^{\text{SH}}$ are orders of magnitude faster due to the underlying FFT. However, $\mathcal{G}^{\text{SH},\psi<180^\circ}$ usually cannot be used at the topography due to the divergence of spherical harmonics (Sansò, 2013). Recently, Bucha (2025) proposed a combined spatial-spectral method that works even at the topography. It integrates near-zone masses up to some ψ_0 (here $\psi_0 = 10^\circ$) by a spatial-domain method (here $\mathcal{G}^T$) and the remaining masses beyond ψ_0 are modeled by a modification of the spectral method after Bucha (2025) (here $\mathcal{G}^{\text{SH}}$). Bucha and Kuhn (2020) suggest that the spherical-harmonic method converges even at the topography as long as integrated are only far-zone masses with sufficiently large distance from evaluation points. According to Eq. (15) of Bucha and Kuhn (2020), ψ_0 should be larger than $\psi_{\text{conv}} = \max(\text{LDEM128})/1727\ \text{km} \approx 0.7^\circ$ to achieve convergence everywhere at the lunar topography. Here, we shall use $\psi_0 = 10^\circ > \psi_{\text{conv}}$. Let us acknowledge that a formal proof of the hypothesis by Bucha and Kuhn (2020) has still not been found, but their numerical experiments and also those from this paper (Section 3.3.3) are consistent with the hypothesis.

Thus, to improve performance, the first term on the right-hand side of Eq. (5) can be split as

$$\begin{aligned} & \mathcal{G}^{T,\psi<180^\circ}_{0..\infty}(\text{LDEM128}_{0..\infty}) = \mathcal{G}^{T,\psi<10^\circ}_{0..\infty}(\text{LDEM128}_{0..\infty}) \\ & + \mathcal{G}^{T,\psi\geq10^\circ}_{0..\infty}(\text{LDEM128}_{0..\infty}) \end{aligned} \tag{6}$$

and subsequently it can be approximated as

$$\begin{aligned} & \mathcal{G}^{T,\psi<180^\circ}_{0..\infty}(\text{LDEM128}_{0..\infty}) \approx \mathcal{G}^{T,\psi<10^\circ}_{0..\infty}(\text{LDEM128}_{0..\infty}) \\ & + \mathcal{G}^{\text{SH},\psi\geq10^\circ}_{0..10800}(\text{LDEM128\_SH}_{0..5400}), \end{aligned} \tag{7}$$

where the notation $\psi < 10^\circ$ and $\psi \geq 10^\circ$ means that integrated are only masses up to and beyond the spherical distance $\psi_0 = 10^\circ$ from each evaluation point, respectively. The truncation degrees of 10,800 and 5400 in $\mathcal{G}^{\text{SH},\psi\geq10^\circ}_{0..10800}(\text{LDEM128\_SH}_{0..5400})$ were chosen such that the approximation errors can be safely neglected yet the computations remain manageable (note that this will require spherical-harmonic transforms up to degree ∼54,000 to avoid the aliasing, see Sections 3.3.2 and 3.3.3 and Bucha 2025). The final RTM formula used to develop LGM2026 therefore reads

$$V^{\mathrm{RTM}} = \mathcal{G}^{T,\psi<10^\circ}_{0..\infty}(\mathrm{LDEM128}_{0..\infty}) + \mathcal{G}^{\mathrm{SH},\psi\geq10^\circ}_{0..10800}(\mathrm{LDEM128\_SH}_{0..5400}) - \mathcal{G}^{\mathrm{SH},\psi<180^\circ}_{0..500}(\mathrm{LDEM128\_SH}_{0..500}) - \mathrm{LF}. \tag{8}$$

Generally, Eq. (8) follows the baseline technique of Hirt et al. (2019a) with two differences to be discussed in Sections 3.2.1 and 3.2.2.

Let us remind that topography band-limited to degree $N > 0$ generates full-spectrum gravity field and that this holds for both spatial- and spectral-domain gravity-forward modeling methods (Hirt and Kuhn, 2014). As a result, the gravity field of, say, LDEM128_SH$_{0..5400}$ covers all harmonics so that $\mathcal{G}^{\mathrm{SH},\psi<180^\circ}_{0..\infty}(\mathrm{LDEM128\_SH}_{0..5400}) = \mathcal{G}^{T,\psi<180^\circ}_{0..\infty}(\mathrm{LDEM128\_SH}_{0..5400})$ (for now, we assume evaluation points above the minimum lunar circumscribing sphere, so that $\mathcal{G}^{\mathrm{SH},\psi<180^\circ}_{0..\infty}$ converges). With spectral methods, it can thus be truncated at degree, say, $2 \times 5400 = 10{,}800$ which is in our notation written as $\mathcal{G}^{\mathrm{SH},\psi<180^\circ}_{0..10800}(\mathrm{LDEM128\_SH}_{0..5400})$ (see Eq. 8).

3.2.1. High-frequency RTM correction

Equation (8) does not include a high-frequency RTM correction term, which is defined as (Rexer et al., 2018)

$$\mathrm{HF} = \mathcal{G}^{\mathrm{SH},\psi<180^\circ}_{501..\infty}(\mathrm{LDEM128\_SH}_{0..500}). \tag{9}$$

In our case, this correction must not be applied, because it is already accounted for by truncating the gravitational effects $\mathcal{G}^{\mathrm{SH},\psi<180^\circ}_{0..500}(\mathrm{LDEM128\_SH}_{0..500})$ at the desired degree of 500. The high-frequency correction is typically required when the gravitational field of LDEM128_SH$_{0..500}$ is evaluated by spatial-domain methods (e.g., prisms or tesseroids), which do not permit to spectrally truncate gravitational effects.

3.2.2. Low-frequency RTM correction

Unlike the RTM baseline technique of Hirt et al. (2019a), our RTM takes into account also the low-frequency correction (see LF in Eq. 8; the study of Hirt et al. 2019a did not require this correction). The purpose of the low-frequency correction is to remove residual signals that are otherwise found in RTM below the resolution of the spherical-harmonic topography (here, degrees up to 500; Rexer et al., 2018). After applying the correction, RTM does not contain any signal power up to degree 500, so that adding RTM to GRGM1200B (Eq. 3) will not tamper the observed GRAIL signals found in GRGM1200B. We discuss two methods to compute the low-frequency RTM correction.

The method A reads

$$\begin{aligned}\mathrm{LF} &= \mathcal{G}^{\mathrm{SH},\psi<180^\circ}_{0..500}(\mathrm{LDEM128}_{0..\infty}) - \mathcal{G}^{\mathrm{SH},\psi<180^\circ}_{0..500}(\mathrm{LDEM128\_SH}_{0..500}) \\ &\approx \mathcal{G}^{\mathrm{SH},\psi<180^\circ}_{0..500}(\mathrm{LDEM128\_SH}_{0..5400}) - \mathcal{G}^{\mathrm{SH},\psi<180^\circ}_{0..500}(\mathrm{LDEM128\_SH}_{0..500}).\end{aligned} \tag{10}$$

That is, the correction represents gravitational signals up to degree 500 which are implied by the residual topography. Clearly, substituting the relation after the equal sign in Eq. (10) into (5) leads to

$$V^{\mathrm{RTM}} = \mathcal{G}^{T,\psi<180^\circ}_{0..\infty}(\mathrm{LDEM128}_{0..\infty}) - \mathcal{G}^{\mathrm{SH},\psi<180^\circ}_{0..500}(\mathrm{LDEM128}_{0..\infty}), \tag{11}$$

which is the sought filtration of the gravitational effects implied by the high-resolution topography LDEM128. This proves that topography-implied gravity can be high-pass filtered exactly also by means of a reference spherical-harmonic topography as long as the low- and high-frequency corrections are applied. The obvious problem is that if N_T and N_G are too high in $\mathcal{G}^{\mathrm{SH},\psi<180^\circ}_{0..N_G}(\mathrm{LDEM128\_SH}_{0..N_T})$, convergence of the spherical-harmonic expansion of the gravitational potential is not guaranteed at the planetary surface. In fact, for realistic bodies and sufficiently high N_T and N_G, the series will likely diverge on the planetary body as shown numerous times in the literature (Hu and Jekeli, 2015; Hirt and Kuhn, 2017; Bucha and Sansò, 2021). In our case, $N_T = N_G = 500$ are low enough to avoid the divergence of spherical harmonics at the lunar surface (see also Section 3.1).

A different approach, hereafter named the method B, was used by Rexer et al. (2018). It consists of two steps: (i) the spherical-harmonic analysis of

$$V^{\mathrm{RTM\ without\ LF}} = \mathcal{G}^{T,\psi<10^\circ}_{0..\infty}(\mathrm{LDEM128}_{0..\infty}) + \mathcal{G}^{\mathrm{SH},\psi\geq10^\circ}_{0..10800}(\mathrm{LDEM128\_SH}_{0..5400}) - \mathcal{G}^{\mathrm{SH},\psi<180^\circ}_{0..500}(\mathrm{LDEM128\_SH}_{0..500}), \tag{12}$$

where $V^{\mathrm{RTM\ without\ LF}}$ is evaluated on a circumscribing sphere passing outside all masses, and (ii) the synthesis of the obtained coefficients up to degree 500.

We shall numerically show in Section 3.4 that both approaches are equivalent. For reasons to be explained later in Section 3.4, we opted for the method B in the LGM2026 development.

3.3. Gravity-forward modeling

Two gravity-forward modeling techniques were used to compute Eq. (8): a spatial-domain technique based on tesseroids (Section 3.3.1) and a spectral-domain technique based on spherical harmonics (Section 3.3.2).

3.3.1. Spatial-domain gravity-forward modeling

We used the tesseroid-based spatial-domain method of Lin et al. (2020) to evaluate $\mathcal{G}^{T,\psi<10^\circ}_{0..\infty}(\mathrm{LDEM128}_{0..\infty})$ from Eq. (8). It calculates the gravitational field of a tesseroid, whose density $\rho(r')$ varies radially with r' as a finite-degree polynomial

$$\rho(r') = \sum_{i=0}^{I} \rho_i\,(r')^i. \tag{13}$$

Once the polynomial density coefficients ρ_i are allowed to vary with latitude φ' and longitude λ', that is, from tesseroid to tesseroid, gravity-forward modeling of lunar topography with 3D variable density is possible.

To represent the density, we used the 1°×1° linear 3D density model by Goossens et al. (2020) with the cap radius of 15° and degree range 250–650. This model provides the surface density $\rho_{\mathrm{surf}}(\varphi', \lambda')$ and its first-order gradient $\rho_{\mathrm{grad}}(\varphi', \lambda')$, so that the density is modeled as

$$\rho(r', \varphi', \lambda') = \rho_{\mathrm{surf}}(\varphi', \lambda') + \rho_{\mathrm{grad}}(\varphi', \lambda')\, z(r', \varphi', \lambda'), \quad (14)$$

where $z(r', \varphi', \lambda') = r_{\mathrm{surf}}(\varphi', \lambda') - r'$ is the depth with respect to the lunar surface $r_{\mathrm{surf}}(\varphi', \lambda')$. By a simple transformation, the polynomial density coefficients from Eq. (13) are obtained as

$$\rho_0(\varphi', \lambda') = \rho_{\mathrm{surf}}(\varphi', \lambda') + \rho_{\mathrm{grad}}(\varphi', \lambda')\, r_{\mathrm{surf}}(\varphi', \lambda') \quad (15)$$

and

$$\rho_1(\varphi', \lambda') = -\rho_{\mathrm{grad}}(\varphi', \lambda'). \quad (16)$$

With the linear density model of Goossens et al. (2020), the order of the radial polynomial density coefficients is $I = 1$. Since density data in the model of Goossens et al. (2020) are missing near the poles (latitudes $|\varphi| \geq 88°$), we used the nearest neighbor interpolation to fill-in the gaps.

The method of Lin et al. (2020) evaluates Newton integral and its derivatives by the Gauss–Legendre quadrature in latitude, longitude and spherical radius. In all three dimensions, we used 11 quadrature nodes for all tesseroids up to $\psi < 0.3°$, 5 quadrature points for tesseroids with $0.3° \leq \psi < 0.5°$, 3 quadrature points if $0.5° \leq \psi < 3°$ and finally 2 quadrature points for $3° \leq \psi < 10°$. We found this setup to be a good compromise between the accuracy (see Section 5.1.3) and computing speed. The parameter related to the 2D adaptive subdivision was 10. The adopted value of Newton's gravitational constant is $G = 6.67430 \times 10^{-11}\ \mathrm{m^3\ kg^{-1}\ s^{-2}}$ (Tiesinga et al., 2021).

For reasons of numerical efficiency, the forward modeling $\mathcal{G}^{T,\psi<10°}_{0..\infty}(\mathrm{LDEM128}_{0..\infty})$ was performed by combining two grids of different resolutions. We used LDEM128 sampled at 128 PPD for all tesseroids with spherical distance $\psi < 0.5°$ from evaluation points. At spherical distances $0.5° \leq \psi < 10°$, we used LDEM128 resampled to 64 PPD. This grid was obtained from the original LDEM128 by a weighted block averaging, with weights being given by the pixel size. To avoid issues associated with the singularity of Newton's kernel and of its derivatives in the case of the surface gravitational maps (see Section 3), the evaluation points were placed 0.1 m above the topography. Our implementation of the tesseroid-based technique is written in the C programming language and employs OpenMP and AVX-512 parallelization techniques to efficiently tackle large-scale forward modeling tasks.

3.3.2. Spectral-domain gravity-forward modeling

The two terms $\mathcal{G}^{\mathrm{SH},\psi<180°}_{0..500}(\mathrm{LDEM128\_SH}_{0..500})$ and $\mathcal{G}^{\mathrm{SH},\psi\geq10°}_{0..10800}(\mathrm{LDEM128\_SH}_{0..5400})$ from Eq. (8) were evaluated by the spherical-harmonic gravity-forward modeling technique of Bucha (2025), which is designed to work with constant, lateral and 3D density models. We shall discuss the computation of both terms separately.

Evaluation of $\mathcal{G}^{\mathrm{SH},\psi<180°}_{0..500}(\mathrm{LDEM128\_SH}_{0..500})$

The term $\mathcal{G}^{\mathrm{SH},\psi<180°}_{0..500}(\mathrm{LDEM128\_SH}_{0..500})$, which we now denote $V^{\mathrm{SH},\psi<180°}_{0..500}(r, \varphi, \lambda)$ in the context of the gravitational potential, was obtained by the equation

$$V^{\mathrm{SH},\psi<180°}_{0..500}(r, \varphi, \lambda) = \frac{\mathrm{GM}}{R} \sum_{n=0}^{500} \left(\frac{R}{r}\right)^{n+1} \times \sum_{m=-n}^{n} \bar{V}_{nm}^{\mathrm{LDEM128\_SH}_{0..500}}\, \bar{Y}_{nm}(\varphi, \lambda), \quad (17)$$

where GM is the product of Newton's gravitational constant G (see Section 3.3.1) and the mass of the Moon $M = 7.34630 \times 10^{22}$ kg (Williams et al., 2014), $R = 1727$ km is the radius of the sphere, to which we referenced LDEM128_SH (see Section 3.2) and $\bar{V}_{nm}^{\mathrm{LDEM128\_SH}_{0..500}}$ are the spherical-harmonic coefficients of the gravitational potential implied by the LDEM128_SH$_{0..500}$ topography. Following Bucha (2025), these coefficients are given as

$$\bar{V}_{nm}^{\mathrm{LDEM128\_SH}_{0..500}} = \frac{2\pi R^3}{M} \sum_{p=1}^{P} \sum_{i=0}^{I} S_{npi}\, \overline{\mathrm{H}\rho}^{(pi)}_{nm}, \quad (18)$$

where

$$S_{npi} = \frac{2}{2n+1} \frac{1}{n+i+3} \binom{n+i+3}{p} \quad (19)$$

and

$$\overline{\mathrm{H}\rho}^{(pi)}_{nm} = \frac{1}{4\pi} \int_{\varphi'=-\frac{\pi}{2}}^{\frac{\pi}{2}} \int_{\lambda'=0}^{2\pi} \mathrm{H}\rho^{(pi)}(\varphi', \lambda')\, \bar{Y}_{nm}(\varphi', \lambda') \times \mathrm{d}\lambda' \cos\varphi' \,\mathrm{d}\varphi' \quad (20)$$

are the spherical-harmonic coefficients of the topographic height-density function

$$\mathrm{H}\rho^{(pi)}(\varphi', \lambda') = \left(\frac{H^{\mathrm{LDEM128\_SH}_{0..500}}(\varphi', \lambda')}{R}\right)^{p} \times \rho_i(\varphi', \lambda')\, R^i. \quad (21)$$

The symbol P is the maximum topography power (see p in Eq. 21) and I is the order of the radial polynomial density coefficients (see Eq. 13). To evaluate Eq. (18), we used $P = 50$ and $I = 1$. While in theory P approaches infinity (see Bucha, 2025), we have checked that $P = 50$

is sufficient to suppress the truncation error at a negligible level for our LDEM128_SH$_{0..500}$ topography (see also Hirt and Kuhn, 2017; Bucha and Kuhn, 2020). The value $I = 1$ is determined by the density model from Eq. (13). Equation (17) was evaluated at the lunar surface and on the circumscribing sphere of the radius 1749 km (see Section 3) in the same way as Eq. (4). Equation (18) was calculated using CHarm.

Evaluation of $\mathcal{G}^{\mathrm{SH},\psi\geq 10^\circ}_{\mathbf{0..10800}}$ (LDEM128_SH$_{\mathbf{0..5400}}$)

The computation of $\mathcal{G}^{\mathrm{SH},\psi\geq 10^\circ}_{0..10800}$(LDEM128_SH$_{0..5400}$) from Eq. (8), here denoted as $V^{\mathrm{SH},\psi\geq 10^\circ}_{0..10800}(r,\varphi,\lambda)$, was slightly different for points at the lunar surface and on the circumscribing sphere.

Let us begin with the circumscribing sphere. In this case, the spherical radius of all points is constant, $r = r_C = 1749$ km. The gravitational potential of far-zone masses ($\psi \geq 10^\circ$) implied by the topography model LDEM128_SH$_{0..5400}$ and truncated at degree 10,800 reads (Bucha, 2025)

$$V^{\mathrm{SH},\psi\geq 10^\circ}_{0..10800}(r_C,\varphi,\lambda) = \frac{\mathrm{GM}}{R} \times \sum_{n=0}^{10800}\sum_{m=-n}^{n} \bar{V}^{\mathrm{LDEM128\_SH}_{0..5400}}_{nm}(r_C,\psi_0,R)\,\bar{Y}_{nm}(\varphi,\lambda), \tag{22}$$

where $\psi_0 = 10^\circ$ and the spherical-harmonic coefficients are given as

$$\bar{V}^{\mathrm{LDEM128\_SH}_{0..5400}}_{nm}(r_C,\psi_0,R) = \frac{2\pi\,R^3}{M} \times \sum_{p=1}^{P}\sum_{i=0}^{I} Q_{npi}(r_c,\psi_0,R)\,\overline{\mathrm{H}\rho}^{(pi)}_{nm}. \tag{23}$$

Here, $Q_{npi}(r_c,\psi_0,R)$ are Molodensky's truncation coefficients (for definition and numerical evaluation, see Bucha, 2025) and $\overline{\mathrm{H}\rho}^{(pi)}_{nm}$ are given by Eq. (20), but this time with $H^{\mathrm{LDEM128\_SH}_{0..5400}}$ instead of $H^{\mathrm{LDEM128\_SH}_{0..500}}$. Since the truncation degrees of the topography and of its implied gravitational potential are now higher compared to Eq. (17) (5400 and 10,800 now vs. 500 and 500 in Eq. 17), we were forced to decrease P from 50 to 10. As will be shown in Section 3.3.3, $P = 10$ is fairly sufficient this time, because now we are dealing with the gravitational potential of far-zone masses only ($\psi \geq 10^\circ$) which is smooth compared to all masses ($\psi < 180^\circ$) in Eq. (17). This is explained by the attenuation of the gravitational field with increasing distance from source (for an example in the spectral domain, see Bucha et al., 2019).

Let us move to the evaluation of $V^{\mathrm{SH},\psi\geq 10^\circ}_{0..10800}$ at the lunar topography with varying spherical radius r. It would be highly impractical to use Eq. (22) now, because the spherical-harmonic coefficients in this equation depend on the spherical radius of the evaluation point (r_C in Eq. 22). This would generally mean a different set of coefficients for each of the $23{,}040 \times 46{,}080 \approx 10^9$ LGM2026 points. To overcome this, Bucha et al. (2019) followed Balmino et al. (2012) and Hirt (2012) and employed the upward/downward continuation from some auxiliary sphere of the radius R_a to the topography with the varying radius $r_{\mathrm{surf}}(\varphi,\lambda)$. This technique is called the gradient approach. For simplicity, let $V = V^{\mathrm{SH},\psi\geq 10^\circ}_{0..10800}$. The gradient approach then reads

$$V(r_{\mathrm{surf}},\varphi,\lambda) = \sum_{k=0}^{K}\frac{1}{k!}\left.\frac{\partial^k V}{\partial r^k}\right|_{r=R_a}(r_{\mathrm{surf}} - R_a)^k. \tag{24}$$

The key to efficiency is to evaluate $\partial^k V/\partial r^k\big|_{r=R_a}$ by FFT-based algorithms and then simply substitute these terms into the truncated Taylor series (24). Note that $\partial^k V/\partial r^k$ requires $\partial^k \bar{V}^{\mathrm{LDEM128\_SH}_{0..5400}}_{nm}(r,\psi_0,R)/\partial r^k$ (see Eq. 22), hence $\partial^k Q_{npi}(r,\psi_0,R)/\partial r^k$ (see Eq. 23), making the evaluation of $V^{\mathrm{SH},\psi\geq 10^\circ}_{0..10800}$ at the lunar surface a non-trivial task. To this end, we used the equations of Bucha (2025), which are valid for any n, p, i and k. To make the truncation errors of the Taylor series negligible, we used $K = 40$. This choice will be justified in a numerical test in Section 3.3.3. Again, CHarm was employed to evaluate Eqs. (22) and (23) together with their radial derivatives.

3.3.3. Approximation errors of Eq. (7)

This section shows that the approximation errors in Eq. (7) are negligible. Since Eq. (7) requires to calculate Eq. (22) at the lunar topography, this validation will also provide a numerical evidence (not a proof though) that Eq. (22) can be used reliably at the lunar topography for $\psi_0 = 10^\circ$ without any signs of the divergence of spherical harmonics.

We calculated $\mathcal{G}^{T,\psi<180^\circ}_{0..\infty}$(LDEM128$_{0..\infty}$) on the left-hand side of Eq. (7) by the tesseroid-based gravity-forward modeling method (Section 3.3.1) using all topographic masses (global integration). These data will serve as a reference for the test. Given that this is too time consuming, the forward modeling was conducted only at 360×719 points of all $23{,}040 \times 46{,}080$ LGM2026 points ($0.5^\circ \times 0.5^\circ$ resolution). Importantly, the input topography and density grids were the same as when evaluating LGM2026 maps, that is, they were sampled at the 128-PPD resolution. The right-hand side of Eq. (7) was obtained simply by extracting the data from LGM2026 intermediate results at the corresponding 360×719 grid.

The comparison of both sides of Eq. (7) will mostly reflect approximations in $\mathcal{G}^{\mathrm{SH},\psi\geq 10^\circ}_{0..10800}$(LDEM128_SH$_{0..5400}$) due to (i) the truncation of the gravitational field quantities to spherical-harmonic degree 10,800, (ii) replacing far-zone masses LDEM128$_{0..\infty}$ by LDEM128_SH$_{0..5400}$, and (iii) truncating the originally infinite series over p and k in Eqs. (23) and (24) at $P = 10$ and $K = 40$, respectively.

Table 1 reports outcomes of the validation at the lunar topography. Discrepancies at the same levels were found also for evaluation points located on the circumscribing sphere while the signals were weaker by one order of magnitude at most. Overall, the discrepancies are negligible compared to the overall error budget of LGM2026 (see Section 5), justifying our preference for the more efficient spherical-harmonic technique.

Table 1
Approximation errors of Eq. (7). Shown are statistics of the reference signals from spatial-domain gravity forward modeling (the left-hand side of Eq. 7) and statistics of the discrepancies of the new approach (the right-hand side). STD stands for the standard deviation.

	Reference signal				Discrepancies			
Quantity	min	max	mean	STD	min	max	mean	STD
V [m^2 s^{-2}]	3.4e+04	4.1e+04	3.6e+04	1.5e+03	−2.9e−02	1.9e−01	8.3e−02	1.6e−02
V^{x} [mGal]	−6.8e+02	1.2e+03	3.8e+00	1.7e+02	−2.1e−02	4.0e−02	4.1e−03	4.4e−03
V^{y} [mGal]	−7.9e+02	7.6e+02	−1.8e−02	1.7e+02	−2.7e−02	3.2e−02	−2.7e−04	5.1e−03
V^{z} [mGal]	−3.3e+03	−1.1e+03	−2.1e+03	2.6e+02	−5.6e−03	1.3e−03	−2.4e−03	5.2e−04
V^{xx} [E]	−5.1e+02	7.2e+02	−1.1e+00	8.4e+01	−1.0e−03	1.6e−03	1.0e−04	1.8e−04
V^{xy} [E]	−3.2e+02	3.7e+02	−8.1e−02	4.6e+01	−1.4e−03	1.4e−03	−1.7e−06	2.3e−04
V^{xz} [E]	−6.3e+02	6.3e+02	3.8e−01	9.5e+01	−4.1e−04	2.1e−04	−4.2e−05	4.4e−05
V^{yy} [E]	−5.3e+02	6.5e+02	−1.3e+00	8.4e+01	−1.4e−03	1.4e−03	−1.7e−05	2.0e−04
V^{yz} [E]	−6.3e+02	6.7e+02	1.5e−01	9.5e+01	−3.2e−04	2.8e−04	2.8e−06	5.2e−05
V^{zz} [E]	−1.2e+03	8.1e+02	2.4e+00	1.4e+02	−8.9e−04	7.6e−04	−8.4e−05	1.4e−04

Considering that the reference values of this test are independent of spherical-harmonic techniques, this validation also proved that Eq. (22) does not show any signs of the divergence effect at the lunar surface and thus it can be used to develop LGM2026.

3.4. Comparison of methods for the low-frequency RTM correction

This section shows that the two independent approaches A and B to the low-frequency RTM correction from Section 3.2.2 lead to comparable results.

In the method A, we used Eq. (18) to get spherical-harmonic coefficients of both terms on the right-hand side of Eq. (10) (after the $\approx$ sign). Subsequently, both sets of coefficients were rescaled from the sphere of the radius $R =$ 1727 km (see Eq. 18) to the circumscribing sphere of the radius 1749 km (for the rescaling procedure, see Barthelmes, 2013). The difference spectrum obtained from the two sets of coefficients represents the spectrum of the low-frequency RTM correction on the circumscribing sphere.

In the method B, we harmonically analyzed $V^{\text{RTM without LF}}$, $V^{\text{z,RTM without LF}}$ and $V^{\text{zz,RTM without LF}}$ (see Eq. 12) at evaluation points placed on the circumscribing sphere. To this end, we used bivariate splines of degree 3 to interpolate the 23,040 × 46,080 LGM2026 grids into the points of the Driscoll–Healy quadrature and subsequently harmonically analyzed the signals up to degree 11,519. To the coefficients obtained from $V^{\text{z,RTM without LF}}$ and $V^{\text{zz,RTM without LF}}$, we applied the well-known relations from the Meissl scheme to get potential coefficients (e.g., Jekeli, 2017). Note that the method B cannot be used with the gravitational grids at the topography, because spherical-harmonic analysis by quadrature methods requires the signal to be given on a sphere to get solid spherical-harmonic coefficients. These solid spherical-harmonic coefficients can then be used to upward/downward continue gravitational quantities as usually. This is not possible with the quadrature methods if data are given at the topography, although it can sometimes be the only solution for practical reasons (see Rexer et al., 2018).

The results from both methods and their differences are shown in Fig. 1. The figure reveals some discrepancies between the two methods in the spectral band from 0 to ∼60 whereas good agreement is seen for degrees ∼61 – 500. We attribute the discrepancies mostly to the method B, particularly to the discretization of the lunar topographic masses and to the approximate evaluation of the gravitational field of a tesseroid by the Gauss–Legendre quadrature (Section 3.3.1). Some portion of the disagreement is, however, also due to the method A, in which we had to replace LDEM128$_{0..\infty}$ by LDEM128_SH$_{0..5400}$ when evaluating Eq. (10). Discrepancies are also seen between the three variants of the method B. For degrees up to 2, the method A agrees the most with the method B when the latter is combined with V whereas the worst agreement is seen for the combination with V^{zz}. This could be explained by the fact that the gravitational potential is more sensitive to low degrees than its first- and second-order radial derivatives. As another feature visible in Fig. 1, the difference spectrum between the method B with V and the method A (the blue dashed line) shows an arch-like pattern. This could be associated with the method B, in which the density varied laterally as a step function of the resolution 1° × 1° resolution, while in the method A, the density was a smooth continuous function. In other words, while the original density data were the same for both methods, they entered both methods differently which might produce the arch-like pattern in their difference spectrum. Note that the spectrum of a mass distributed over a spherical rectangle (here 1° × 1° density pixels) follows the same arch-like pattern (Pollack, 1973). Overall, Fig. 1 reveals that the signal power of the low-frequency correction is one or more orders of magnitude weaker than the reference signal from GRAIL.

The coefficients of the low-frequency correction can be used to correct RTM signals. This is possible for the grids residing both at the lunar surface and on the circumscribing sphere. No divergence effect of spherical harmonics (at a detectable level) is expected at the lunar surface, since the low-frequency RTM correction is in our case truncated at degree 500 by definition. From the two methods, we

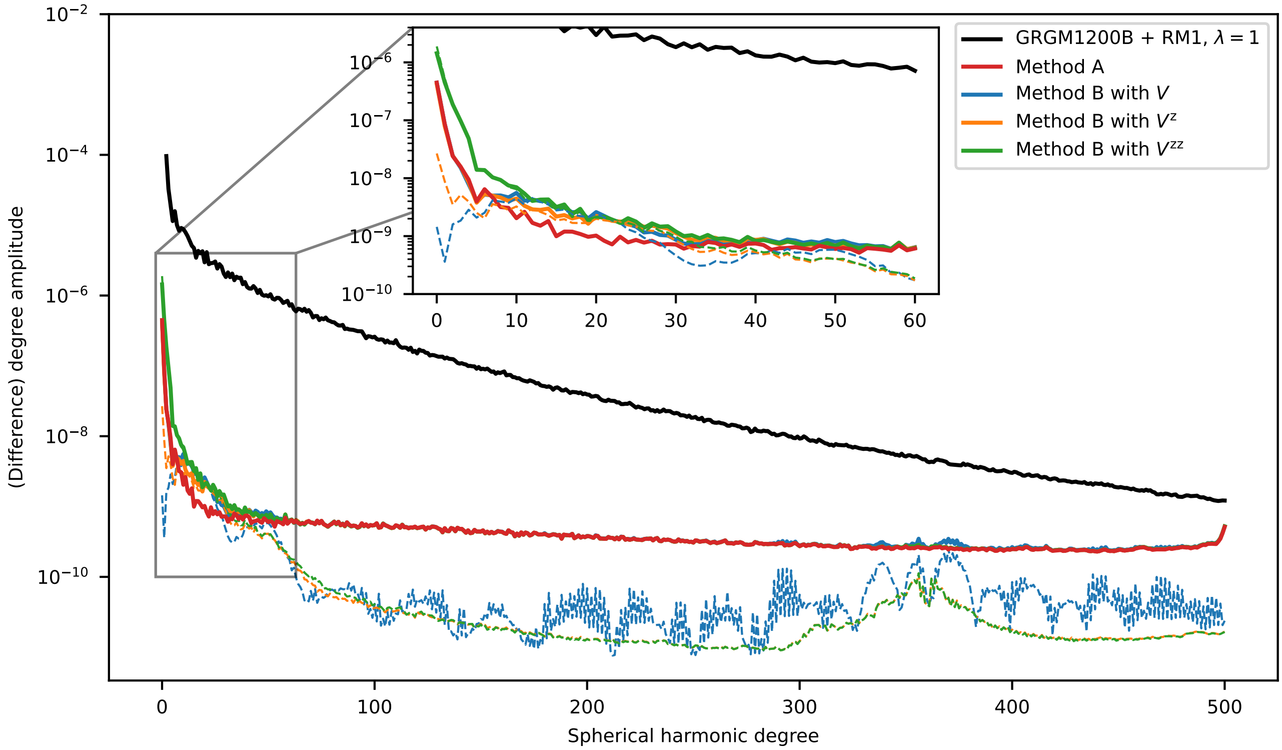

Figure 1: Low-frequency RTM corrections from the methods A and B (all shown in solid lines). For a comparison, the GRAIL gravitational signal from GRGM1200B + RM1, $\lambda = 1$ is shown for degrees $2-500$ (degrees 0 and 1 are omitted in this case in order not to overload the figure). The dashed lines show difference degree amplitudes between the methods A and B. The GRGM1200B + RM1, $\lambda = 1$ model was rescaled to our circumscribing sphere to make it consistent with the other signals. All models use the same GM, which is here taken from GRGM1200B + RM1, $\lambda = 1$.

opted for the method B in the LGM2026 development. The reason is that it removes the signal that is actually found in our RTM grids in the spectral band 0 – 500. We used the method B combined with V to correct the RTM signal of the gravitational potential, the method B with V^{z} to correct all three elements of the gravitational vector and the method B with V^{zz} to correct all six elements of the gravitational tensor. Different sets of coefficients were used with the gravitational potential, vector and tensor in order to improve the removal of low-degree signals, as all three quantities respond to gravity-forward modeling errors differently. Note that if RTM is applied only at the topography, as frequently done in practice, the grids on the circumscribing sphere are not available. In this case, the method A seems to be a viable alternative to correct RTM for the low-frequency error.

As an example, Fig. 2 shows the low-frequency RTM correction (method B with V^{z}) for V^{z} evaluated at the lunar surface and on the circumscribing sphere. By removing this signal from our RTM grids $V^{\mathrm{z,RTM\ without\ LF}}$, we mitigate an interference of artificial RTM signals with GRAIL observations when computing Eq. (3). The $1° \times 1°$ rectangles that are visible in the figure are explained by the original $1° \times 1°$ density grids.

All LGM2026 quantities at the lunar surface and on the circumscribing sphere were corrected for the low-frequency RTM signals.

3.5. Conversion to spherical-harmonic coefficients

The LGM2026 maps are represented as 2D grids. For some applications, however, a spherical-harmonic representation of LGM2026 may be desirable. This sections describes the conversion of LGM2026 maps into an external solid spherical-harmonic expansion.

For the same reasons as with the low-frequency correction method B (Section 3.4), only the LGM2026 grids residing on the circumscribing sphere are suitable for the harmonic analysis. From the ten gravitational quantities of LGM2026, we have harmonically analyzed V and also V^{z} and V^{zz}, because of their simple spectral relation with respect to the gravitational potential V (the Meissl scheme). The remaining quantities that include horizontal derivatives could be analyzed using specialized harmonic analysis methods (e.g., Martinec and Einšpigel, 2018), but this not followed here. We conducted the spherical-harmonic analysis up to degree 11,519 using the Driscoll–Healy quadrature (Driscoll and Healy, 1994). Since LGM2026 grid points do not coincide with the points of the quadrature (offset by a half of the LGM2026 pixel size in both directions), we have interpolated the LGM2026 grids to the quadrature points using bivariate splines of degree 3. After the harmonic analysis, the coefficients obtained from V^{z} and V^{zz} were transformed into the coefficients of the gravitational potential using the Meissl scheme.

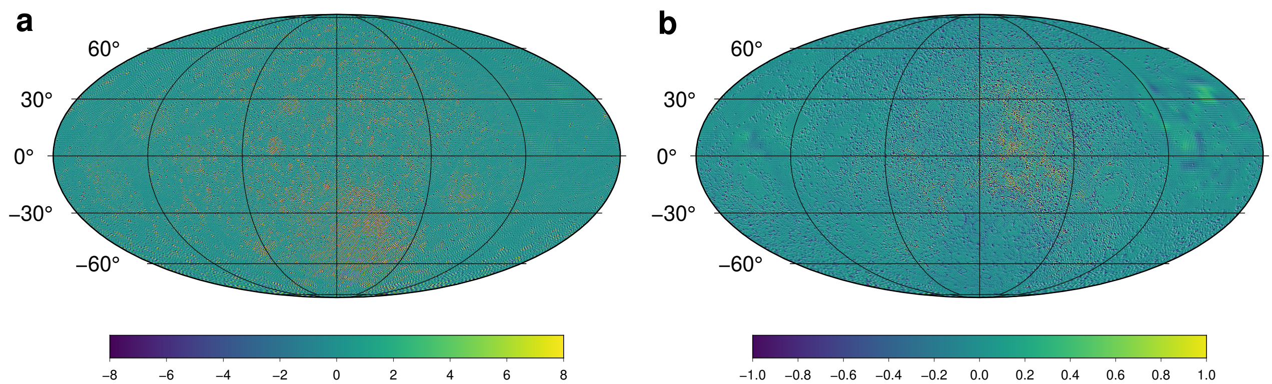

Figure 2: Low-frequency RTM correction for V^z in mGal at the lunar surface (a) and on the circumscribing sphere (b). The statistics of the low-frequency correction (min/max/mean/root mean square, all in mGal) are −9.5e+01/7.7e+01/−7.2e−02/4.1e+00 for the lunar topography and −7.3e+00/7.3e+00/−7.4e−02/3.0e−01 for the circumscribing sphere. The maps are centered at the 180° meridian.

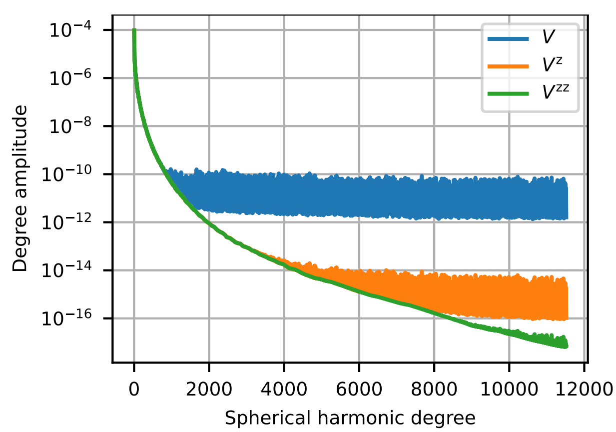

Figure 3: Degree amplitudes obtained by harmonically analyzing V, V^z and V^{zz} on the circumscribing sphere. Harmonic degrees 0 and 1 are omitted for visualization purposes.

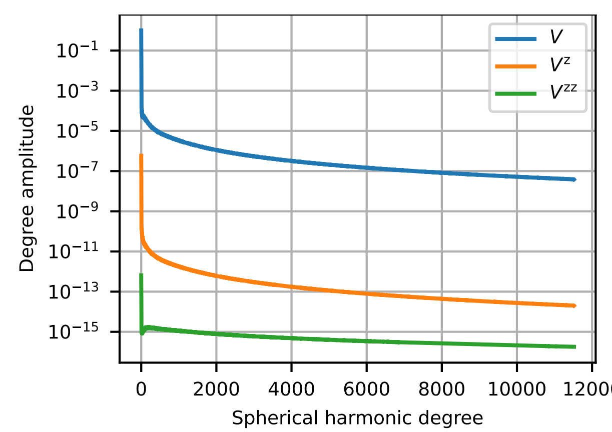

Figure 4: Spectrum of the V (dimensionless), V^z (units m^{-1}) and V^{zz} (units m^{-2}) surface grids assuming the data are signals on the sphere of the radius 1749 km. All coefficients are normalized by the GM and $R = 1749$ km constants. This time, the Meissl scheme is not applied for V^z and V^{zz}.

Fig. 3 shows the spectra of the three quantities. The coefficients from the gravitational potential V are seen to suffer from noise after degree ∼600, making them unusable in this harmonic range. This is caused by our spatial-domain gravity-forward modeling technique (see Section 3.3.1). While we tailored its parameters for evaluation at the topography, they are clearly not suitable for the subtle variations of the gravitational potential on the circumscribing sphere, where the gravitational field is weaker. As the signal content amplifies in high degrees with the order of the radial derivative of the gravitational potential, the range of degrees affected by the noise moves beyond ∼2500 and ∼8500 with V^z and V^{zz}, respectively. The final spherical-harmonic coefficients were obtained by (i) averaging the solutions from V, V^z and V^{zz} in degrees 0 – 500, (ii) averaging V^z and V^{zz} in degrees 501 – 2250 and (iii) taking the coefficients from V^{zz} in degrees 2251 – 11,519. These are the coefficients that will be validated with respect to GRAIL in Section 5.2.

To check for the presence of noise in the LGM2026 grids that reside at the topography, we can simply assume that they are square-integrable functions on a sphere and perform *surface* spherical-harmonic analysis of these grids. Although this procedure does not lead to solid spherical-harmonic coefficients of the gravitational field that could be used in the traditional way, it can reveal the presence of noise. Fig. 4 confirms that the surface grids do not contain noise in the studied spectral bandwidth. This could be explained by the fact that the gravitational field is stronger at the lunar surface compared to the circumscribing sphere, hence it is easier to capture with our spatial-domain gravity-forward modeling.

4. Results

The main product of LGM2026 are maps of the lunar gravitational potential, vector and tensor at the lunar surface and on its circumscribing sphere, all sampled at the 128-PPD spatial resolution. The maps show quantities of the gravitational field, meaning they do not take into account the centrifugal field or the normal gravity field. The coordinate system adopted for all LGM2026 spatial data is the Moon's principal axes coordinate system. As a representative example of all LGM2026 maps, we show in Fig. 5 the maps of the gravitational vector at the lunar surface.

For a more detailed demonstration, we selected the south polar region, because it is significant for lunar exploration due to the possible presence of water ice (Fisher et al., 2017; McClanahan et al., 2024). This is also the region where 13 candidate Artemis locations have been identified for possible human landing. Fig. 6 shows the gravitational acceleration (magnitude of the gravitational vector) over this area as predicted by LGM2026, LGM2011 and the spherical-harmonic model GRGM1200B + RM1, $\lambda = 1$ to degrees 500 and 900. Two deficiencies of the spherical-harmonic model are clearly visible. If its truncation degree is low, the omission error causes the wavy pattern in Fig. 6c. If the truncation degree is high, the signal is overwhelmed by the downward continuation errors and by the divergence of spherical harmonics which leads to spurious oscillations in Fig. 6d. By comparison, LGM2026 (Fig. 6a) and LGM2011 (Fig. 6b) do not suffer from these effects, as they model also the high-frequency gravitational signals and do not rely on spherical harmonics in short scales. Figure 6e shows the gravitational acceleration at the 13 candidate Artemis sites as determined by the four models. Over most stations, LGM2011 predicts largest gravitational acceleration whereas GRGM1200B + RM1, $\lambda = 1$ to degree 500 yields the lowest value. LGM2026 predictions are typically in between LGM2011 and GRGM1200B + RM1, $\lambda = 1$ to degree 900. A possible explanation for the systematically largest values in LGM2011 could be its constant density of 2800 kg m^{-3} (the surface density in LGM2026 varies from $\sim$2375 to $\sim$2495 kg m^{-3} over this region and increases with depth) or the pre-GRAIL spherical-harmonic gravitational model SGM100i (Goossens et al., 2011) used in LGM2011 to degree 70. In the absence of observed surface gravitational data, it is impossible to assess which of the four models performs the best in the south polar region. It can be concluded though that the predictions of the gravitational acceleration at the 13 candidate Artemis sites differ by 104 mGal at maximum and that the degree-900 spherical-harmonic model features artificial oscillations over low-elevated topography. Finally, we acknowledge that we truncated GRGM1200B at degree 900 instead of its maximum degree 1200 for two reasons. First, to suppress high-frequency GRAIL noise (see Goossens et al., 2020), which is disproportionally amplified when the series is evaluated at regions of low elevations. Second, to mitigate the divergence of spherical harmonics at the lunar surface (see Section 3.1). When expanded to degree 1200, the artificial oscillations from Fig. 6d are further amplified and the maximum difference with respect to the degree-900 solution reaches 31 mGal in absolute value at the 13 sites (the ranges remain the same except for Site 5, where the new range is 37 mGal).

Data published along with LGM2026 include (i) the 3D position of the LGM2026 data points, (ii) spherical-harmonic coefficients of the lunar gravitational potential up to degree 11,519 (see Section 3.5) and (iii) maps of the residual gravitational field beyond degree 500.

5. Accuracy

This section analyzes commission errors of LGM2026 (Section 5.1) and evaluates the model with respect to satellite gravity from GRAIL (Section 5.2), surface gravity from the Apollo missions (Section 5.3) and modeled gravity from LGM2011 (Section 5.4).

5.1. Error assessment

Three major contributors to LGM2026 errors are: (i) the long-wavelength term V^{GGM} from Eq. (3) (Section 5.1.1), (ii) the lunar topography model LDEM128 (Section 5.1.2) and (iii) the spatial- and spectral-domain gravity-forward modeling techniques (Sections 5.1.3 and 5.1.4, respectively). A summary of these error analyses will be provided in Section 5.1.5.

5.1.1. Errors of GRGM1200B

This section analyzes LGM2026 errors caused by the spherical-harmonic model GRGM1200B.

Using the 100 clones of the Kaula-constrained GRGM1200B (Goossens et al., 2020), we propagated the errors of GRGM1200B onto the topography and the circumscribing sphere following Sabaka et al. (2014). The characteristics of the errors are reported in Table 2. At the topography, the errors are typically below 0.02 m^2 s^{-2}, 0.4 mGal and 1.1 E for the gravitational potential, the gravitational vector and the gravitational tensor, respectively (1 E $=$ 10^{-9} s^{-2}). On the circumscribing sphere, the errors are smaller by about one to two orders of magnitude. As discussed by Goossens et al. (2020), the errors of GRGM1200B are calibrated, but it is difficult to assess whether they properly reflect the true errors.

Even if the scaling factor is unknown or biased, the error propagation realistically captures relative spatial relations of the errors. The errors of V^{z} are shown in Fig. 7. For the other quantities, the errors follow the same spatial pattern, so are not shown. At the lunar surface, the largest errors are observed over low-elevated areas (e.g., the South Pole–Aitken basin) whereas highlands are associated with the smallest errors. This is explained by the downward continuation errors, which generally increase with the distance between the satellites and the topography. On the circumscribing sphere, dominant are latitudinal stripes, which are related to the constellation of the GRAIL satellites. The errors are largest in the equatorial area and smallest in the polar areas, reflecting the satellite ground tracks.

5.1.2. Errors of LDEM128

This section estimates the contribution of LDEM128 errors to LGM2026. Neumann (2024) does not provide error estimates for LDEM128. However, within the $\pm 60°$ latitudinal range, LDEM128 is derived from SLDEM2015 sampled at 256 PPD (Barker et al., 2016). According to Barker et al. (2016), the vertical accuracy of the 512-PPD version of SLDEM2015 is typically $\sim$3 to 4 m. Considering

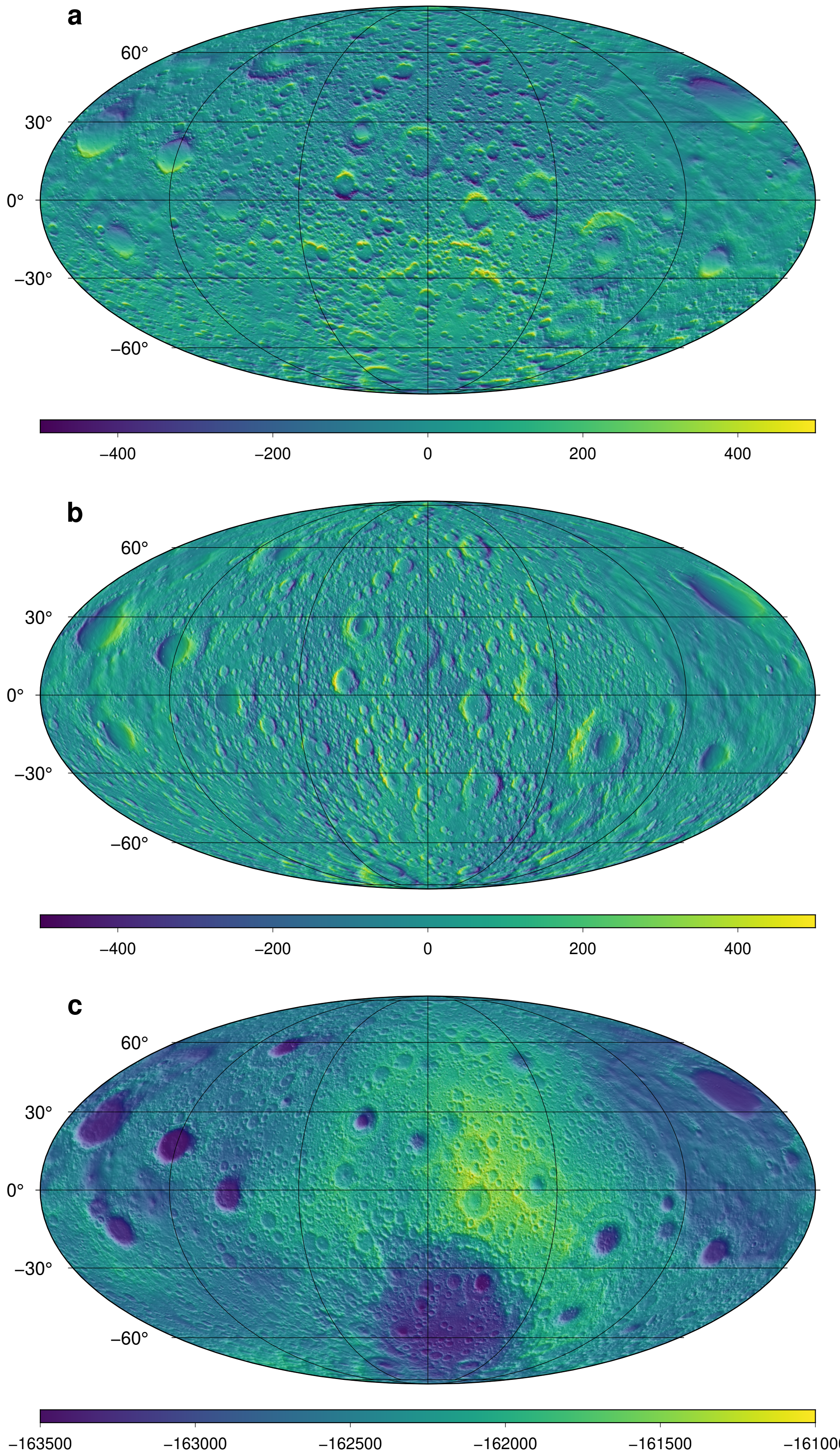

Figure 5: LGM2026 maps of the gravitational vector elements V^{x} (a), V^{y} (b) and V^{z} (c) at the lunar surface (mGal). The maps are downsampled for visualization purposes and are centered at the 180° meridian.

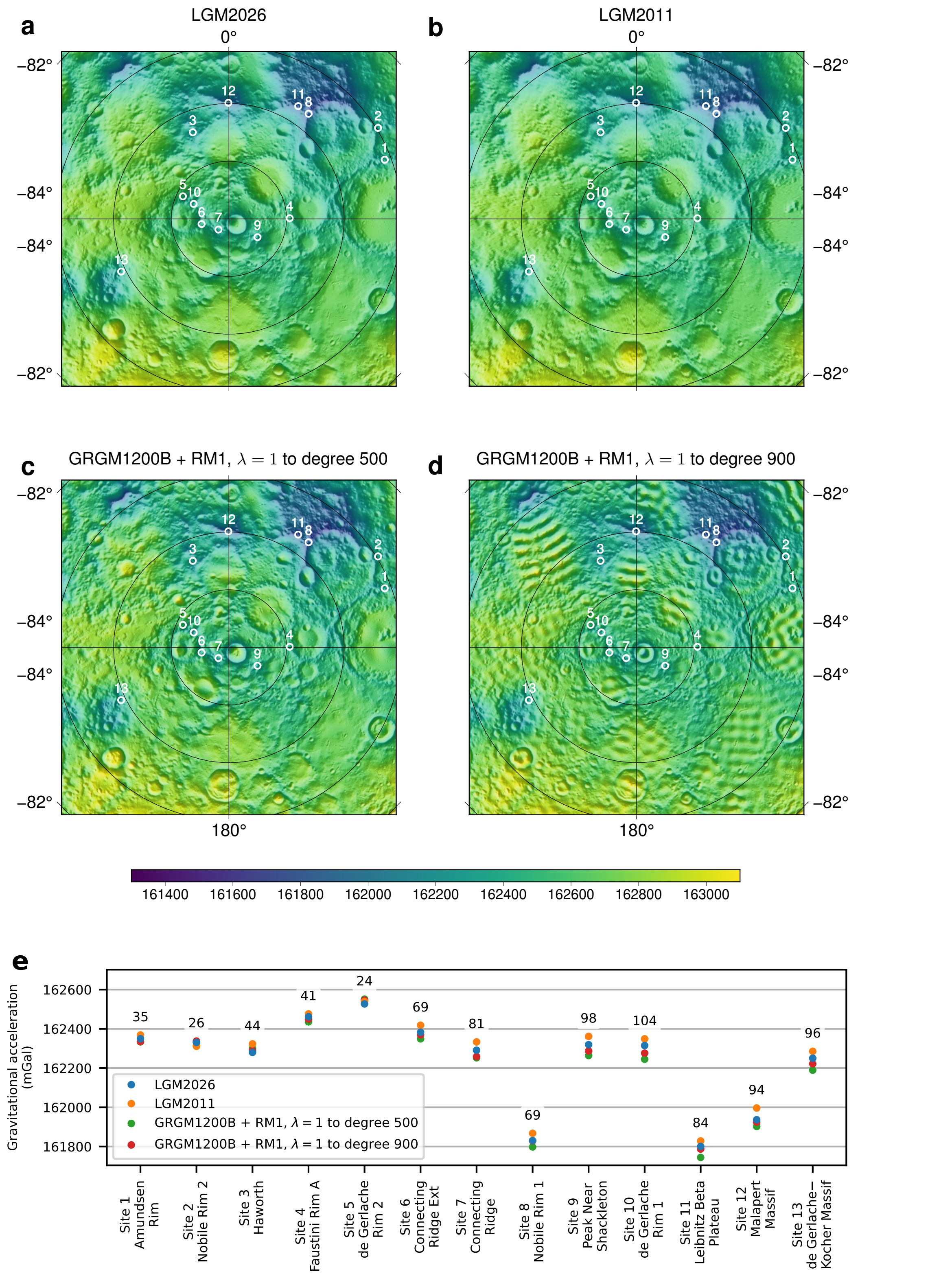

Figure 6: Gravitational acceleration (mGal) over the south polar region from LGM2026 (a), LGM2011 (b) and GRGM1200B + RM1, $\lambda = 1$ to degrees 500 (c) and 900 (d). LGM2011 is plotted in the Mean-Earth/Polar-Axis coordinate system while the remaining maps use the PA coordinates. The 13 points represent candidate Artemis locations for possible human landing (coordinates taken from Goossens et al. 2025 and transformed to PA for LGM2026 and GRGM1200B). LGM2026 and LGM2011 are not shown in their full resolution due to the size of the plotted area (see Fig. 13 for smaller region maps in full resolution). (e) Gravitational acceleration at the 13 stations. The values above the dots indicate the maximum differences between the predictions in mGal. The centrifugal acceleration was removed from LGM2011 to get the gravitational acceleration (Hirt and Featherstone, 2012).

Table 2
Errors of V^{GGM} (Eq. 4) obtained by error propagation of GRGM1200B up to degree 500 onto 1920×3840 grids (5.625 arcmin) residing at the topography level and on the circumscribing sphere. The evaluation points are a subset of LGM2026 grid points.

	Topography			Circumscribing sphere		
Quantity	min	max	90th percentile	min	max	90th percentile
V [m^2 s^{-2}]	1.6e−04	9.5e−02	1.6e−02	6.5e−05	1.9e−03	5.5e−04
V^{x} [mGal]	2.3e−03	1.7e+00	2.5e−01	4.0e−04	3.9e−02	8.3e−03
V^{y} [mGal]	2.7e−03	1.9e+00	3.4e−01	4.4e−04	3.2e−02	1.1e−02
V^{z} [mGal]	3.7e−03	2.6e+00	4.2e−01	6.9e−04	4.6e−02	1.4e−02
V^{xx} [E]	5.7e−03	3.8e+00	5.7e−01	9.2e−04	8.8e−02	1.8e−02
V^{xy} [E]	3.5e−03	2.4e+00	3.9e−01	6.5e−04	3.5e−02	1.2e−02
V^{xz} [E]	6.4e−03	4.6e+00	6.9e−01	1.1e−03	9.8e−02	2.1e−02
V^{yy} [E]	6.8e−03	4.6e+00	8.3e−01	1.0e−03	7.4e−02	2.5e−02
V^{yz} [E]	7.7e−03	5.4e+00	9.1e−01	1.2e−03	8.1e−02	2.8e−02
V^{zz} [E]	1.0e−02	7.0e+00	1.1e+00	2.0e−03	1.1e−01	3.5e−02

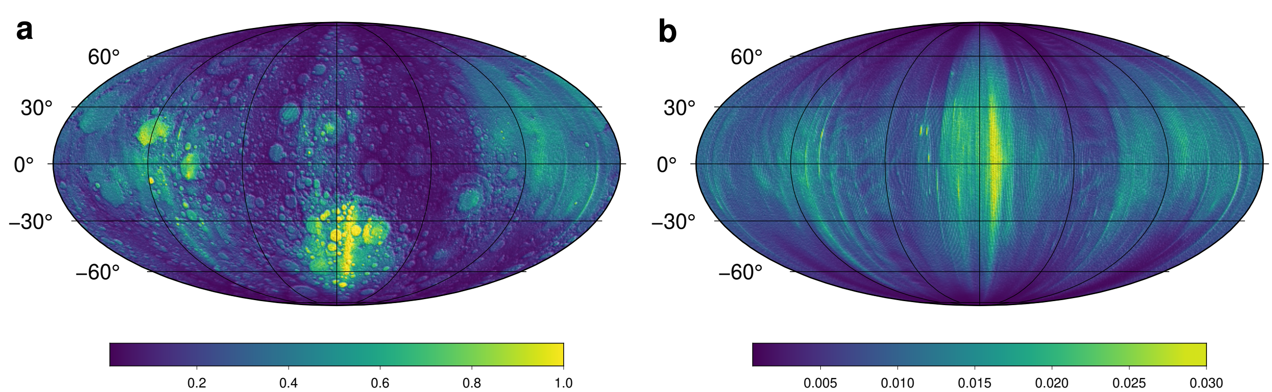

Figure 7: Errors of $V^{\mathrm{z,GRAIL}}$ in mGal at the topography (a) and on the circumscribing sphere (b). The maps are centered at the 180° meridian.

the downsampling to 128 PPD and Fig. 1 of Barker et al. (2016), we shall assume that the accuracy of LDEM128 is 8 m.

LDEM128 errors propagated into LGM2026 in two ways: through spatial-domain gravity-forward modeling $\mathcal{G}^{T,\psi<10^\circ}_{0..\infty}$(LDEM128$_{0..\infty}$) in Eq. (8) and through the radius of evaluation points in Eq. (4) in the case of the grids at the lunar surface.

LDEM128 errors in Eq. (8)

Given that rigorous error propagation for high-resolution gravity-forward modeling in the spatial domain is barely possible, we shall use the Monte Carlo method to estimate the errors of $\mathcal{G}^{T,\psi<10^\circ}_{0..\infty}$(LDEM128$_{0..\infty}$) that are due to the LDEM128 errors. We generated 100 artificial topography models by adding random errors from the Gaussian distribution to LDEM128, assuming zero mean and variance of 64 m^2. In the absence of information on the spatial autocorrelation of the LDEM128 errors, we assumed no spatial correlation. The density is assumed errorless for now. All 100 topography models were forward-modeled using the tesseroid-based approach from Section 3.3.1, keeping the same parameters as during the LGM2026 development. Since spatial-domain gravity-forward modeling is the most time consuming part of all LGM2026 computations, it is unrealistic to conduct 100 forward-modeling runs using all LGM2026 points. Therefore, we chose three representative study areas (Fig. 8). Area 1 (Fig. 8a) is located in the highlands near the equator and includes the highest topography features (mean surface density ∼2280 kg m^{-3}). Area 2 (Fig. 8b) is located in the South Pole–Aitken basin and includes the topography of the lowest elevations (mean surface density ∼2380 kg m^{-3}). Area 3 (Fig. 8c) is located in the flat Oceanus Procellarum mare (mean surface density ∼2720 kg m^{-3}). The results of the error analysis are summarized in Tables 3, 4 and 5, respectively. Clearly, the errors depend both on the topography and its density. Generally, the standard deviations stay mostly below 0.2 m^2 s^{-2} for V, 1 mGal for V^{z} and about 200 E for V^{zz}. The standard deviations for the horizontal components of the gravitational vector and tensor are typically one to two orders of magnitude smaller than that for V^{z} and V^{zz}.

We applied the Monte Carlo method also at points on the circumscribing sphere. For brevity, we do not provide detailed statistics, but overall, the errors dropped by one to two orders of magnitude for the gravitational potential and for the gravitational vector and three to four orders of magnitude for the gravitational tensor.

Our estimate of the standard deviation for V^{z} can be checked by a simplistic model of the Bouguer plate. If LDEM128 is radially in error with respect to the true

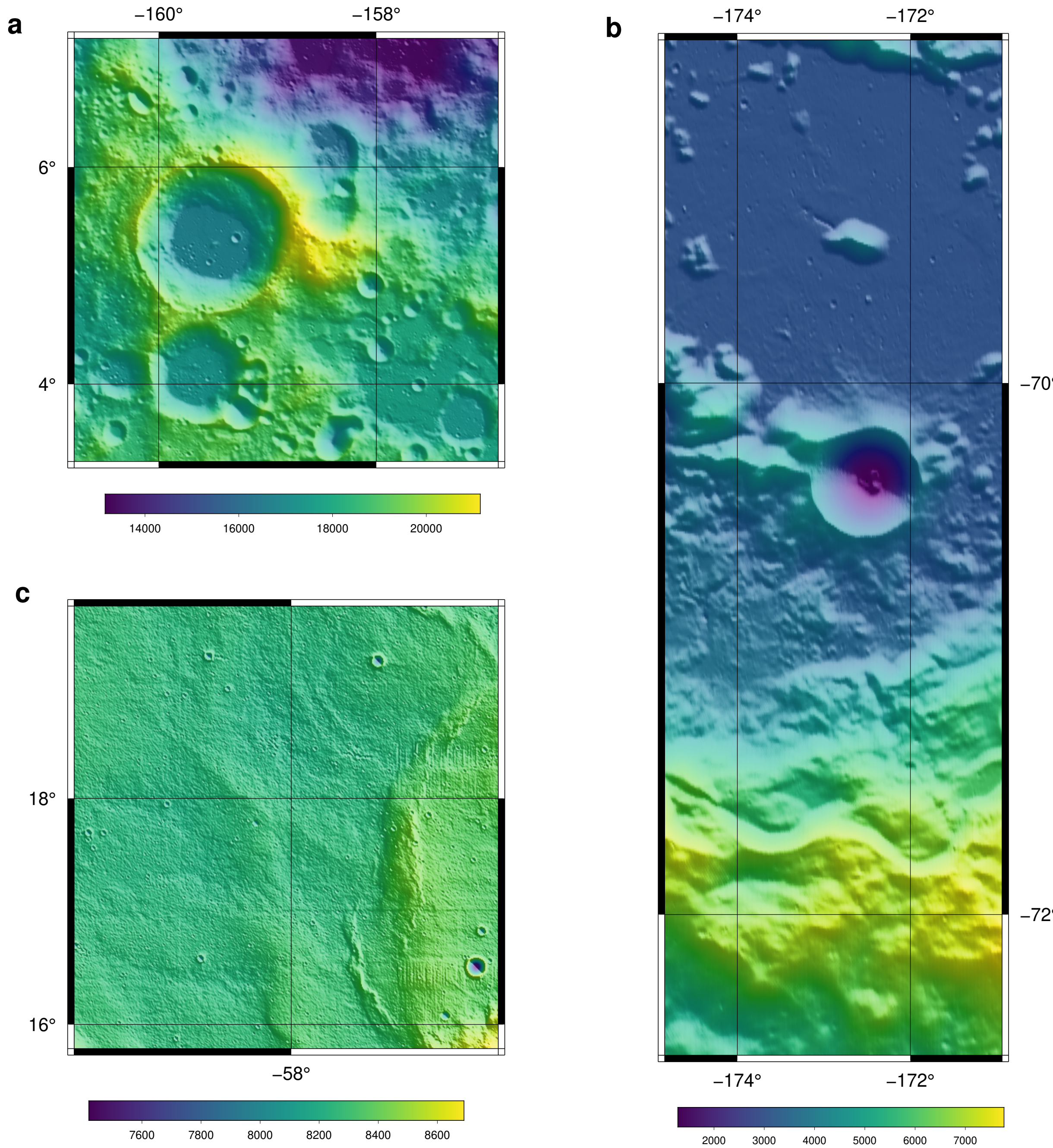

Figure 8: Topography (m) over the three study areas for experiments from Sections 5.1.2 and 5.1.3: area 1 (a), area 2 (b) and area 3 (c). The resolution of the maps is 128 PPD, but the evaluation points were downsampled by a factor of 10 in the experiments. The grids of the gravitating masses were used in their original resolution of 128 PPD.

topography by $\Delta h = 8$ m, the Bouguer plate predicts the change in V^{z} to be $2\pi\, G\, \rho\, \Delta h = 0.8$ mGal using the mean density of the three study areas $\rho = 2460 \mathrm{kg\ m^{-3}}$. This is within reasonable agreement with our estimate of 1 mGal.

In the previous error analysis, we assumed the 3D variable density distribution is errorless. While it is straightforward to model the density noise based on the error analysis of the density grids by Goossens et al. (2020), doing so would significantly skew our error estimates. This can be explained as follows. Clearly, the uncertainty of the linear density model increases with depth. Since our topography model is referenced to an internal sphere of the radius 1727 km (see Section 3.2), the largest topographic height is about 21,150 m. This is therefore the height of the highest tesseroid used in gravity-forward modeling $\mathcal{G}^{T,\psi<10^{\circ}}_{0..\infty}(\mathrm{LDEM128}_{0..\infty})$. Along such long distance, the density uncertainty can significantly increase with the depth, producing large uncertainties of the gravitational quantities. But this is unrealistic for LGM2026,

Table 3
Propagation of LDEM128 errors to gravitational quantities for spatial-domain gravity-forward modeling in the study area 1 (highlands near the equator, the highest lunar topography point included). The study area is given by 50×50 point grid with the $0.078125°$ spacing covering the latitudes from $3.4°$ to $7.2°$ and longitudes from $199.2°$ to $203.1°$ (subset of LGM2026 grid points). Shown are the minimum standard deviations, the maximum standard deviations and the 90th percentile.

Quantity	min	max	90th percentile
V [m^2 s^{-2}]	9.8e−02	2.0e−01	1.8e−01
V^{x} [mGal]	2.0e−01	5.1e−01	3.5e−01
V^{y} [mGal]	2.0e−01	5.2e−01	3.5e−01
V^{z} [mGal]	1.4e−01	1.6e+00	7.7e−01
V^{xx} [E]	1.6e+01	7.1e+01	4.7e+01
V^{xy} [E]	6.3e+00	1.5e+01	1.1e+01
V^{xz} [E]	1.2e+01	8.2e+01	2.0e+01
V^{yy} [E]	1.6e+01	6.8e+01	4.7e+01
V^{yz} [E]	1.2e+01	6.1e+01	1.9e+01
V^{zz} [E]	3.0e+01	1.2e+02	7.5e+01

Table 4
The same as Table 3 but for the study area 2 (the South Pole–Aitken basin, the lowest lunar topography point included) given by 50×50 point grid with the $0.078125°$ spacing covering the latitudes from $-68.6°$ to $-72.4°$ and longitudes from $185.2°$ to $189.0°$ (subset of LGM2026 grid points)

Quantity	min	max	90th percentile
V [m^2 s^{-2}]	7.3e−03	7.6e−02	5.8e−02
V^{x} [mGal]	7.5e−02	2.1e−01	1.5e−01
V^{y} [mGal]	1.8e−01	6.4e−01	5.0e−01
V^{z} [mGal]	1.4e−01	1.5e+00	1.0e+00
V^{xx} [E]	1.1e+01	3.6e+01	2.5e+01
V^{xy} [E]	2.8e+00	1.2e+01	7.2e+00
V^{xz} [E]	8.7e−01	4.1e+01	2.2e+01
V^{yy} [E]	2.8e+01	3.2e+02	2.0e+02
V^{yz} [E]	1.6e+01	2.1e+02	8.8e+01
V^{zz} [E]	2.9e+01	2.9e+02	2.0e+02

because due to the RTM technique, forward-modeled are in fact only residual masses, that is, the masses between LDEM128 and LDEM128_SH$_{0..500}$ (see Section 3.2). Considering these actually used residual masses, the largest tesseroid height is 2658 m while the 90th percentile is only 391 m. Thus, the forward-modeled masses that entered LGM2026 never exceeded the ± 2658 m range, so the error analysis must reflect this.

Goossens et al. (2020) do not provide error analysis for the density model used in the LGM2026 development, only for a different version (see their Section 5.3). For the other version, they estimated the mean surface density error at 11 kg m^{-3} and the mean error of surface density gradients at 0.0023 kg m^{-4}. Generally, the uncertainties are larger than the average over maria (see Fig. 18 of Goossens et al., 2020), but RTM gravitational signals are weak in these regions due to the flat topography. The surface density errors reach up to 1 % of the surface density itself while the density gradient errors reach about 20 % of the signal (both 90th percentiles). Using

Table 5
The same as Table 3 but for the study area 3 (Oceanus Procellarum, flat topography) given by 50×50 point grid with the $0.078125°$ spacing covering the latitudes from $15.9°$ to $19.7°$ and longitudes from $300.0°$ to $303.8°$ (subset of LGM2026 grid points)

Quantity	min	max	90th percentile
V [m^2 s^{-2}]	6.1e−02	1.0e−01	8.6e−02
V^{x} [mGal]	2.0e−01	3.8e−01	3.3e−01
V^{y} [mGal]	1.8e−01	3.9e−01	3.5e−01
V^{z} [mGal]	5.2e−01	1.6e+00	1.0e+00
V^{xx} [E]	1.4e+01	7.5e+01	6.3e+01
V^{xy} [E]	5.2e+00	1.1e+01	9.9e+00
V^{xz} [E]	3.1e+00	5.0e+01	6.1e+00
V^{yy} [E]	1.2e+01	7.9e+01	6.9e+01
V^{yz} [E]	4.0e+00	6.0e+01	7.6e+00
V^{zz} [E]	2.4e+01	1.4e+02	1.2e+02

the linear relationship between density and the gravitational field, we expect density errors to propagate into the RTM signals at a level of approximately 1 to 2 % relative to the signal strength. Considering the magnitudes of RTM signals are 1.1 m^2 s^{-2} for V, 29 to 43 mGal for $\vec{g}$ and 82 to 280 E for V (all 90th percentiles), we estimate the LGM2026 errors due to the density model to be typically below 0.02 m^2 s^{-2} for V, 0.6 to 0.9 mGal for $\vec{g}$ and 1.6 to 5.6 E for $\mathbf{V}$.

LDEM128 errors in Eq. (4)

LDEM128 defines the vertical position of the grid, at which LGM2026 provides the lunar surface gravitational field (more precisely, the points reside 0.1 m above LDEM128, see Section 3). The vertical uncertainty of LDEM128 thus propagates into the gravitational quantities at the lunar surface when synthesizing GRGM1200B. After linearization, the error propagation can be conducted using vertical gradients of the gravitational quantities. Here, we shall use the mean gradients at the lunar surface for simplicity.

Considering the mean value of V^{z} from LGM2026 is roughly -162500 mGal at the lunar surface, an error in the spherical radius of 8 m (see Section 5.1.2) propagates into an error of 13 m^2 s^{-2} in V. With the mean value of $V^{\mathrm{zz}} = 1830$ E from the LGM2026 surface maps, an error of 1.5 mGal in V^{z} can be expected at the distance of 8 m. Given that V^{xz} and V^{yz} are about one order of magnitude smaller than V^{zz}, the errors of V^{x} and V^{y} will also be an order of magnitude smaller compared to the errors of V^{z}. The error estimation for the gravitational tensor is difficult, because LGM2026 does not show the third-order gravitational gradients. However, the approximate relation $V^{\mathrm{zzz}} \approx -6 \frac{G\,M}{(1{,}737{,}400\ \mathrm{m})^4} = -3.2 \times 10^{-12}$ m^{-1} s^{-2} (see Section 3.3 for the values of G and M) leads to an error of 0.026 E for V^{zz}. Since the gravitational field of planetary objects typically varies more in the radial direction than in the horizontal directions (see, for instance, the magnitudes at the scales of Fig. 5), the error estimates for the remaining elements of the gravitational tensor will not exceed the 0.026 E error for V^{zz}.

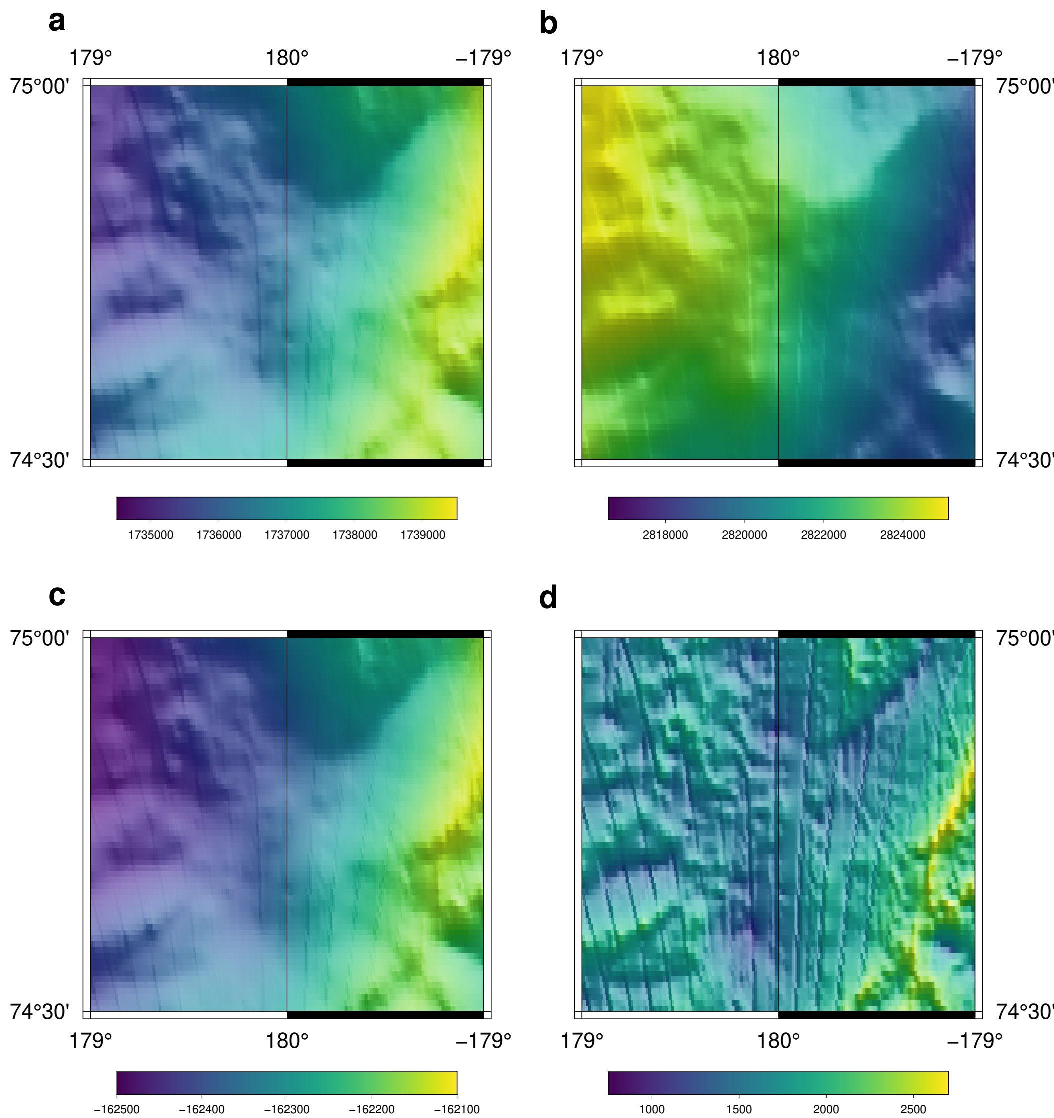

Figure 9: Artifacts in LDEM128, which propagated into LGM2026. Spherical radius of the lunar topography in meters (a), the gravitational potential in $\mathrm{m}^2\ \mathrm{s}^{-2}$ (b), the V^z element of the gravitational vector in mGal (c) and the V^{zz} element of the gravitational tensor in E (d).

Relative to the other error sources, the error of the vertical position of the evaluation point grid is by far the most significant for the gravitational potential and is safely negligible for the gravitational tensor. For the gravitational vector, it is comparable to the other sources of errors. Importantly, these error estimates are tied to the gravitational quantities of LGM2026. Once the concept of the disturbing field is introduced (e.g., Hofmann-Wellenhof and Moritz, 2005), so that one works with quantities such as the disturbing potential, gravity anomalies or deflections of the vertical, then the errors due to the vertical position of evaluation points fall a few orders of magnitude (e.g., three or four orders for the disturbing potential) and thus become safely negligible compared to other error sources. This is explained by the fact that the magnitudes of the vertical gradients of disturbing field quantities are smaller by a few orders compared to the gradients of gravitational quantities. For instance, the magnitude of the radial derivative of the disturbing potential (negative gravity disturbance in spherical approximation) at the lunar surface is typically at the order of $\sim 10^2$ mGal, while the magnitude of the radial derivative of the gravitational potential is $\sim 1.6 \times 10^5$ mGal (see Fig. 5c).

Artifacts in LDEM128

LDEM128 is a state-of-the-art model of the lunar topography. This does not mean, however, that it is free of artifacts or errors. Artifacts in LDEM128 propagated into LGM2026 in at least two ways. First, they affected the V^{GGM} term in Eq. (4) through the radial coordinate of evaluation points. Second, they affected spatial-domain gravity-forward modeling when evaluating $\mathcal{G}_{0..\infty}^{T,\psi<10^\circ}(\mathrm{LDEM128}_{0..\infty})$ in Eq. (8). An example of LGM2026 artifacts caused by LDEM128 is shown in Fig. 9.

Table 6

Impact of the Gauss–Legendre quadrature orders on the accuracy of spatial-domain gravity-forward modeling. The orders are here denoted as $O_1/O_2/O_3/O_4$, where the order O_1 is used for tesseroids up the to spherical distance $\psi < 0.3^\circ$ from the evaluation points, O_2 is used for $0.3^\circ \leq \psi < 0.5^\circ$, O_3 is used for $0.5^\circ \leq \psi < 3^\circ$ and O_4 is used for $3^\circ \leq \psi < 10^\circ$ (see also Section 3.3.1). The table reports statistics of the discrepancies between the solution with 11/5/3/2 (used in the LGM2026 development) and two higher-order solutions. The max column shows the maximum error in absolute value, STD stands for the standard deviation and the 90th percentile is shown for the absolute value of the discrepancies. The statistics are reported for the study area 1 from Section 5.1.2.

	Gauss–Legendre quadrature 15/9/7/6				Gauss–Legendre quadrature 17/11/9/8			
Quantity	max	mean	STD	90th percentile	max	mean	STD	90th percentile
V [m^2 s^{-2}]	8.6e−03	−5.6e−03	1.9e−03	7.6e−03	8.6e−03	−5.6e−03	1.9e−03	7.5e−03
V^{x} [mGal]	3.5e+00	−9.0e−02	4.8e−01	7.8e−01	4.0e+00	−1.2e−01	6.5e−01	1.1e+00
V^{y} [mGal]	3.2e+00	1.7e−02	4.9e−01	7.3e−01	3.7e+00	2.4e−02	6.6e−01	1.0e+00
V^{z} [mGal]	1.8e+00	−1.5e−01	1.9e−01	3.8e−01	1.7e+00	−8.2e−02	1.9e−01	3.1e−01
V^{xx} [E]	5.5e+02	1.0e+01	3.3e+01	3.3e+01	6.7e+02	2.5e+01	5.4e+01	7.4e+01
V^{xy} [E]	9.1e+01	−1.5e+00	1.7e+01	2.9e+01	9.0e+01	−1.6e+00	1.9e+01	3.2e+01
V^{xz} [E]	4.3e+02	2.1e+01	1.0e+02	1.8e+02	4.4e+02	2.5e+01	1.2e+02	2.2e+02
V^{yy} [E]	4.8e+02	9.9e+00	3.5e+01	2.8e+01	6.1e+02	2.4e+01	5.8e+01	6.2e+01
V^{yz} [E]	4.6e+02	−4.3e+00	1.0e+02	1.7e+02	5.0e+02	−5.2e+00	1.2e+02	2.2e+02
V^{zz} [E]	5.4e+02	−2.0e+01	4.8e+01	6.5e+01	6.7e+02	−4.9e+01	7.9e+01	1.5e+02

Removal of the artifacts from LDEM128 prior to gravity field modeling—as done, for instance, in SRTM2gravity (Hirt et al., 2019b)—would certainly be desirable, but this is not a straightforward task due to the nature of the artifacts. A decision has therefore been made to use LDEM128 as is. The gravitational potential is the least affected by the artifacts, while the gravitational tensor is affected the most (relative to the signal strength).

5.1.3. Errors of spatial-domain gravity-forward modeling

This section estimates the internal accuracy of the spatial-domain gravity-forward modeling $\mathcal{G}^{T,\psi<10^\circ}_{0..\infty}$(LDEM128$_{0..\infty}$). This validation is necessary, because the method requires some empirical choices, most notably to choose the orders of the Gauss–Legendre quadrature (see Section 3.3.1).

In this internal validation, we compared the gravitational effects $\mathcal{G}^{T,\psi<10^\circ}_{0..\infty}$(LDEM128$_{0..\infty}$) from LGM2026 with respect to two solutions relying on higher orders of the Gauss–Legendre quadrature. We chose two higher-order solutions to illustrate that further increasing the quadrature orders would likely lead to marginal improvements only. For the same reasons as in Section 5.1.2, the numerical experiment is conducted over the three study areas from Fig. 8. The results of the test are reported in Tables 6, 7 and 8. Generally, the errors are the largest over the rugged area 1, which features the highest peaks of the lunar topography. Over the flat topography of medium heights in area 3, the errors are the smallest. Somewhere in between are the errors over the area 2, which is rugged but its elevations are the smallest of the entire lunar surface.

Overall, we conclude that the accuracy is typically at the order 10^{-3} m^2 s^{-2} or better for the gravitational potential, 1 mGal or better for the gravitational vector and 100 E or better for the gravitational tensor. Compared to the error sources from Sections 5.1.1 and 5.1.2, the errors of the gravitational potential are safely negligible, while the errors of gravitational vector and tensor are roughly at the same level as the other error sources.

We repeated the experiment also on the circumscribing sphere, but do not provide detailed statistics for the sake of brevity. Compared to the already reported errors at the lunar topography, the errors of the gravitational potential remained at the same order of magnitude, the errors of the gravitational vector dropped by one to three orders of magnitude and the errors of the gravitational tensor dropped by three to five orders of magnitude. Thus, for the LGM2026 maps on the circumscribing sphere, these errors reach for all quantities similar magnitudes compared to the other error sources.

5.1.4. Errors of spectral-domain gravity-forward modeling

We consider the internal errors of spectral-domain gravity forward modeling in $\mathcal{G}^{\mathrm{SH},\psi<180^\circ}_{0..500}$(LDEM128_SH$_{0..500}$) (see Eq. 8) negligible compared to the other error sources. This is because it is well-known from the literature (e.g., Hirt and Kuhn, 2014; Hirt et al., 2016; Hirt and Kuhn, 2017; Rexer, 2017; Hirt et al., 2019b; Bucha and Sansò, 2021; Bucha, 2025) that this method evaluates gravitational field quantities accurately as long as (i) a sufficiently large number of topography powers is employed (here 50 powers, see Section 3.3.2), (ii) the spectral content of the topography powers $p > 1$ found beyond the resolution of the input topography is properly taken into account as done in our computations and (iii) divergence of spherical harmonic is not present or is negligible. In that case, it can evaluate, for instance, the gravitational vector with a global root mean square error at the order of a few μGal or even less (see the references above).

Table 7
The same as Table 6 but for the study area 2.

Quantity	Gauss–Legendre quadrature 15/9/7/6 max	mean	STD	90th percentile	Gauss–Legendre quadrature 17/11/9/8 max	mean	STD	90th percentile
V [m^2 s^{-2}]	2.7e−04	−1.4e−05	2.9e−05	3.8e−05	2.8e−04	−1.5e−05	3.0e−05	4.0e−05
V^{x} [mGal]	4.9e−01	1.1e−02	5.9e−02	8.8e−02	4.9e−01	1.1e−02	5.6e−02	7.8e−02
V^{y} [mGal]	8.6e−01	−4.6e−03	1.1e−01	1.7e−01	1.2e+00	−7.7e−03	1.2e−01	2.0e−01
V^{z} [mGal]	7.5e−01	2.4e−02	9.4e−02	1.3e−01	8.2e−01	2.8e−02	1.0e−01	1.4e−01
V^{xx} [E]	1.3e+02	−3.2e+00	1.6e+01	2.4e+01	1.3e+02	−4.2e+00	1.6e+01	2.2e+01
V^{xy} [E]	3.0e+01	−4.5e−03	2.8e+00	3.1e+00	3.0e+01	4.2e−02	2.7e+00	3.1e+00
V^{xz} [E]	1.3e+02	−2.7e+00	1.9e+01	2.7e+01	1.2e+02	−2.1e+00	1.9e+01	2.9e+01
V^{yy} [E]	3.6e+02	1.6e+01	4.8e+01	6.0e+01	4.0e+02	1.9e+01	5.1e+01	7.6e+01
V^{yz} [E]	5.3e+02	4.3e+00	5.9e+01	9.5e+01	5.5e+02	6.4e+00	7.2e+01	1.2e+02
V^{zz} [E]	3.6e+02	−1.2e+01	4.7e+01	5.9e+01	4.0e+02	−1.5e+01	5.0e+01	7.2e+01

Table 8
The same as Table 6 but for the study area 3.

Quantity	Gauss–Legendre quadrature 15/9/7/6 max	mean	STD	90th percentile	Gauss–Legendre quadrature 17/11/9/8 max	mean	STD	90th percentile
V [m^2 s^{-2}]	5.3e−04	−3.4e−05	2.2e−05	4.2e−05	6.4e−04	−3.5e−05	2.6e−05	4.0e−05
V^{x} [mGal]	3.9e−01	−1.0e−03	2.7e−02	2.5e−02	4.0e−01	−1.2e−03	2.7e−02	2.5e−02
V^{y} [mGal]	4.7e−01	−2.4e−03	3.2e−02	3.0e−02	4.3e−01	−2.1e−03	3.1e−02	3.1e−02
V^{z} [mGal]	1.5e+00	4.3e−03	7.0e−02	1.1e−02	1.5e+00	5.1e−03	7.6e−02	2.0e−02
V^{xx} [E]	1.2e+02	5.9e−01	7.7e+00	5.9e+00	1.3e+02	5.0e−01	8.1e+00	7.3e+00
V^{xy} [E]	4.3e+01	−4.6e−04	1.7e+00	6.2e−01	4.1e+01	1.1e−03	1.6e+00	5.6e−01
V^{xz} [E]	1.9e+02	2.7e−01	6.0e+00	3.6e+00	2.1e+02	2.7e−01	6.6e+00	2.9e+00
V^{yy} [E]	1.4e+02	8.4e−01	8.3e+00	5.9e+00	1.4e+02	8.0e−01	8.5e+00	7.6e+00
V^{yz} [E]	1.7e+02	1.1e−01	6.8e+00	5.0e+00	2.1e+02	−1.6e−02	7.7e+00	4.3e+00
V^{zz} [E]	2.4e+02	−1.4e+00	1.5e+01	1.0e+01	2.5e+02	−1.3e+00	1.5e+01	1.3e+01

Based on our error analysis from Section 3.3.3, we also neglected the internal errors of $\mathcal{G}^{\mathrm{SH},\psi\geq 10^\circ}_{0..10800}$ (LDEM128_SH$_{0..5400}$) (see Eq. 8).

5.1.5. Conclusions from the error assessment

By error propagation of the uncertainties from Sections 5.1.1 to 5.1.4 (the 90th percentiles), the commission error of the surface LGM2026 maps is estimated at 13 m^2 s^{-2} for the gravitational potential, 2 mGal for the gravitational vector, 250 E for the diagonal tensor elements and a few tens of E for the off-diagonal tensor elements. Near rims of craters, over rugged or low-elevated topography or when LDEM128 artifacts are present, worse accuracy should be expected for the gravitational vector and especially for the gravitational tensor.

The bulk of the 13 m^2 s^{-2} error of the gravitational potential is due to the uncertainty of the vertical position of the LGM2026 surface grid. Therefore, if the normal gravitational potential is subtracted from the LGM2026 gravitational potential, the uncertainty of the disturbing potential will be about three to four orders of magnitude better compared to the gravitational potential. This is relevant, for instance, when computing the lunar geoid or quasigeoid. On the other hand, the uncertainties of the gravitational vector and tensor reflect mostly errors of our spatial-domain gravity-forward modeling and errors of the topography model LDEM128. Therefore, uncertainties of the disturbing field quantities derived from the gravitational vector (e.g., gravity anomaly or gravity disturbance) and from the gravitational tensor (e.g., the disturbing tensor) remain at the same levels as for the gravitational quantities, because other error sources dominate in this case.

The errors of the LGM2026 grids on the circumscribing sphere are expected to be smaller than the errors at the lunar surface at least by two orders of magnitude for the gravitational potential, one order of magnitude for the gravitational vector and three orders of magnitude for the gravitational tensor. This error reduction is due to the assumed deterministic radius of the circumscribing sphere as well as due to the increased distance from gravitating masses.

5.2. Evaluation using satellite gravity from GRAIL

We evaluated the LGM2026 maps on the circumscribing sphere with respect to the GRAIL model GRGM1200B + RM1, $\lambda = 1$ (shortened to GRGM1200B in this section). Unlike its Kaula-constrained version, on which LGM2026 relies (see Section 2), this variant incorporates a topography-based constraint after degree 600 and thus is more accurate in

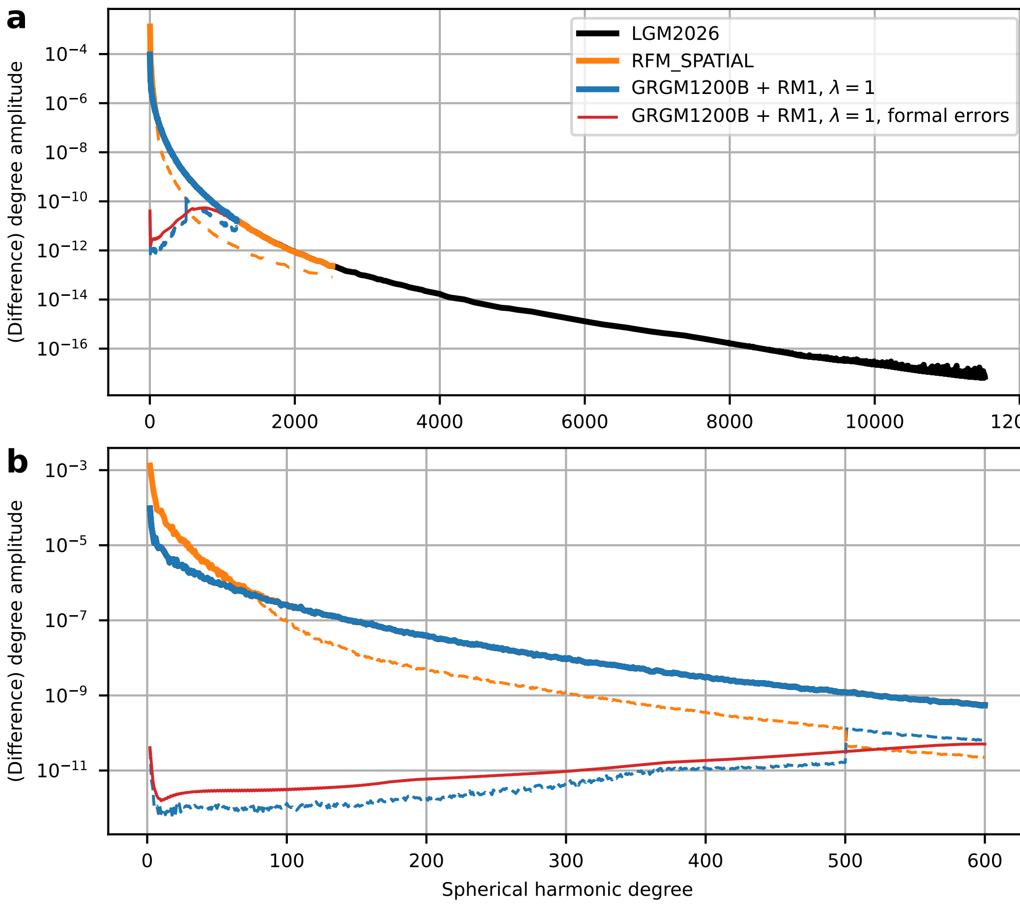

Figure 10: (a) Dimensionless degree amplitudes of LGM2026, GRGM1200B + RM1, $\lambda = 1$, and RFM_SPATIAL (solid lines) and their differences with respect to LGM2026 (dashed lines). The red line represents formal errors of GRGM1200B + RM1, $\lambda = 1$ that were published along with that model. Harmonic degrees 0 and 1 are omitted from the plot for better visualisation. All coefficients were rescaled to the same scaling constants and all degree amplitudes refer to the sphere of the radius 1749 km which passes outside the Moon in mass-free space. (b) Zoom-in to harmonic degrees 2 – 600.

this spectral band. A validation with respect to a GRAIL-based model is useful despite the fact that LGM2026 incorporates GRAIL data through the Kaula-constrained GRGM1200B. Such a validation can (i) reveal interference of V^{RTM} with V^{GGM} in Eq. (3) in harmonics up to degree 500, (ii) check the transition from GRAIL to RTM between degrees 500 and 501 and (iii) it can validate LGM2026 a few tens of degrees beyond degree 500, where LGM2026 relies solely on the forward-modeled gravity but the GRAIL model still incorporates real gravitational observations.

The differences between LGM2026 and GRGM1200B are shown in Fig. 10. In low degrees up to 500, LGM2026 closely follows GRGM1200B as expected thanks to the low-frequency RTM correction (see Section 3.4). Even though LGM2026 relies exclusively on the Kaula-constrained GRGM1200B up to degree 500, the two models are not identical in this band probably because of the interpolation that was necessary to harmonically analyze LGM2026 (see Sections 3.4 and 3.5). Still, the discrepancies are below the formal errors of GRGM1200B. Beyond degree 500, the difference degree amplitudes between LGM2026 and GRGM1200B experience a sudden jump, likely due to the missing GRAIL gravity observations in LGM2026 after degree 500. Beyond degree, say, 700 or 800, validation of LGM2026 with respect to GRGM1200B faces limitations due to the noise in GRGM1200B (see the red curve approaching the signal in Fig. 10a).

At higher degrees, LGM2026 can be compared with respect to RFM_SPATIAL (Šprlák et al., 2020). This model is expanded to degree 2519 and was derived by gravity-forward modeling of the lunar crust using LOLA topography and a 3D density. RFM_SPATIAL neither includes gravitational contributions of masses below the crust nor it directly relies on GRAIL data (only indirectly through the 3D density model and crust-mantle boundary, which were estimated from GRAIL). Given that RFM_SPATIAL does not reflect masses below the crust, LGM2026 expectedly does not match it in long wavelengths (degrees below a few hundreds). But in higher degrees, where the gravitational field of the lunar crust dominates in LGM2026, the two models agree reasonably well. Specifically, the differences between the models at degree 501 are almost two orders of magnitude smaller than the signal. Beyond this degree, the discrepancies grow relative

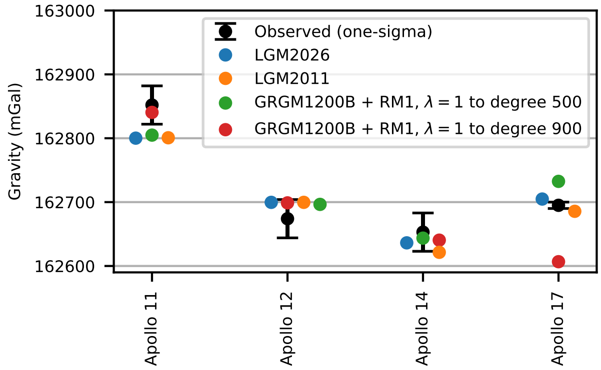

Figure 11: Gravity predictions at the Apollo sites compared to the observed gravity. The centrifugal acceleration was added to LGM2026 and to GRGM1200B + RM1, $\lambda = 1$ using the angular velocity $\omega = 2.6617073 \times 10^{-6}$ rad s^{-1} (Wieczorek, 2015). The observed gravity values, their uncertainties and the site coordinates were taken from Hirt and Featherstone (2012). For LGM2026 and GRGM1200B, the coordinates were transformed to the PA coordinate system. Some of the dots are off-centered in the horizontal direction for visualization purposes.

to the signal strengths, but keep the signal-to-noise ratio above 1, indicating a reasonably good agreement.

Beyond degree 2519, LGM2026 remains unvalidated because of the lack of higher-degree spherical-harmonic lunar gravitational models. It is evident though that after degree ~8500, noise overwhelms the signal (note that this holds only for the LGM2026 maps on the circumscribing sphere and not for the LGM2026 surface maps, see Section 3.5).

5.3. Evaluation using surface gravity from the Apollo missions

At the lunar surface, the accuracy assessment is limited by the scarcity of surface gravity observations. Available validation data consist of four surface gravity values determined by the Apollo 11, 12, 14 and 17 missions (for the data, see, e.g., Hirt and Featherstone, 2012). The topography near the Apollo 11, 12 and 14 sites is mostly flat, resulting only in small variations of the gravitational field in these regions. When combined with the large uncertainty of 30 mGal, the limitations of the validation at these three sites are clear. Conversely, the Apollo 17 site is located in a more rugged valley and the uncertainty of the gravity is reduced to 5 mGal. Figure 11 compares gravity predictions by LGM2026, LGM2011 and GRGM1200B to the observed gravity. All predictions fall within the two-sigma uncertainties except for the Apollo 17 site, where only LGM2026 and LGM2011 satisfy the two-sigma criterion. Notably, the Apollo 17 site happens to be the most challenging validation site due to its complex topography and low gravity uncertainty, making it suitable for validation of short-scale gravity signals. Although our evaluation using gravity from Apollo missions evidently lacks robustness, LGM2026 seems to be in agreement with existing models and especially with LGM2011.

5.4. Evaluation using gravity modeled from LGM2011

Finally, we compared the gravitational acceleration from LGM2026 and LGM2011 globally over the entire lunar surface (Fig. 12). The discrepancies between the two models range from −220 to 203 mGal with the standard deviation of 23 mGal. Largest discrepancies are generally seen in long wavelengths, often over the mascons. We attribute this mostly to the spherical-harmonic models representing long wavelengths in LGM2026 (the Kaula-constrained GRGM1200B to degree 500) and in LGM2011 (the pre-GRAIL model SGM100i to degree 70). We acknowledge that Hirt and Featherstone (2012) published also the RTM component of LGM2011 and therefore the outdated SGM100i signals in LGM2011 could be updated by some recent GRAIL model, though only up to degree 70. In short wavelengths, some discrepancies between LGM2026 and LGM2011 are also seen which could be attributed to the different resolutions of the background topography models (128 PPD vs. 20 PPD, respectively). Overall, the observed standard deviation of 23 mGal falls within the declared uncertainties of LGM2026 (a few mGal) and LGM2011 (a few tens of mGal; Hirt and Featherstone, 2012).

Visualization of LGM2026 and LGM2011 in their full resolutions over a small region in the South Pole–Aitken basin is provided in Fig. 13. Thanks to its ~6-times higher resolution, LGM2026 reveals gravitational field features that are invisible to LGM2011.

Finally, we would like to point out the limitations of our evaluation of LGM2026 using LGM2011. The LGM2026 maps are expressed in the Moon's principal axes coordinate system. On the other hand, the topography-implied gravity from LGM2011 relies on a topography model from the LRO mission, which is given in the Mean-Earth/Polar-Axis coordinate system. The difference between these coordinate systems can reach 875 m (Neumann, 2024). To be able to perform a simple pixel-to-pixel comparison, we neglected the fact that both models are expressed in different coordinate systems. Given the 1.5-km resolution of LGM2011 at the equator, this seems to be permissible within reasonable error limits. Another option would be to transform LGM2011 pixel-by-pixel to the Moon's principle axes coordinate system, leading to irregularly distributed pixels, and then to interpolate into a regular grid. In this way, the coordinate systems would match, but this approach produces another kind of errors, namely interpolation errors.

6. Applications

LGM2026 could be beneficial to theoretical studies as well as to engineering applications that are sensitive to fine scales of the lunar gravitational field. *The maps of the gravitational potential* can help to establish a physically meaningful lunar height system (Tenzer et al., 2018) to study, for instance, gravity-driven mass movements or basalt flow direction (Wieczorek, 2015). *The maps of the gravitational vector* can be useful for gravity predictions at

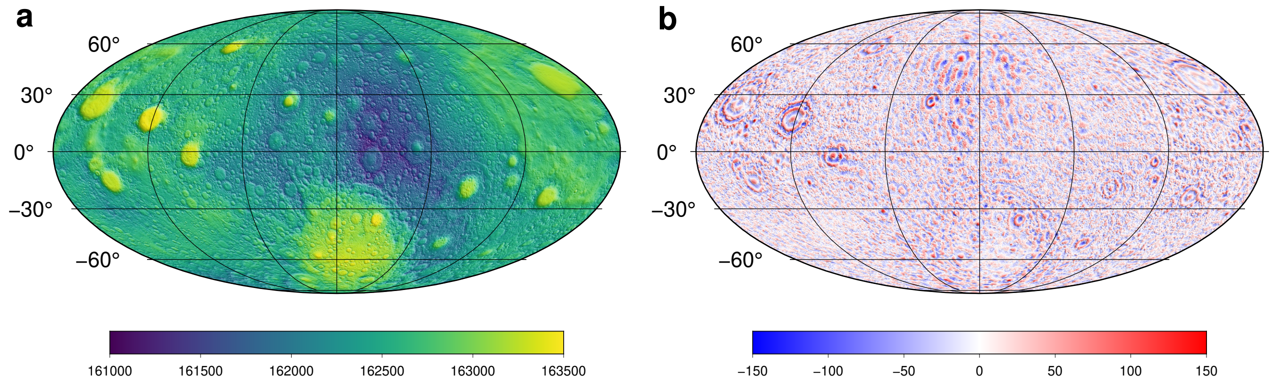

Figure 12: (a) Gravitational acceleration from LGM2026 (block averaged to the $0.05° \times 0.05°$ resolution to match LGM2011) and (b) its difference with respect to LGM2011. Before the comparison, the centrifugal acceleration was removed from the surface gravity of LGM2011 to get the gravitational acceleration. The statistics of the differences (min/max/mean/standard deviation) are $-220.3/203.2/0.5/22.8$. All values in mGal.

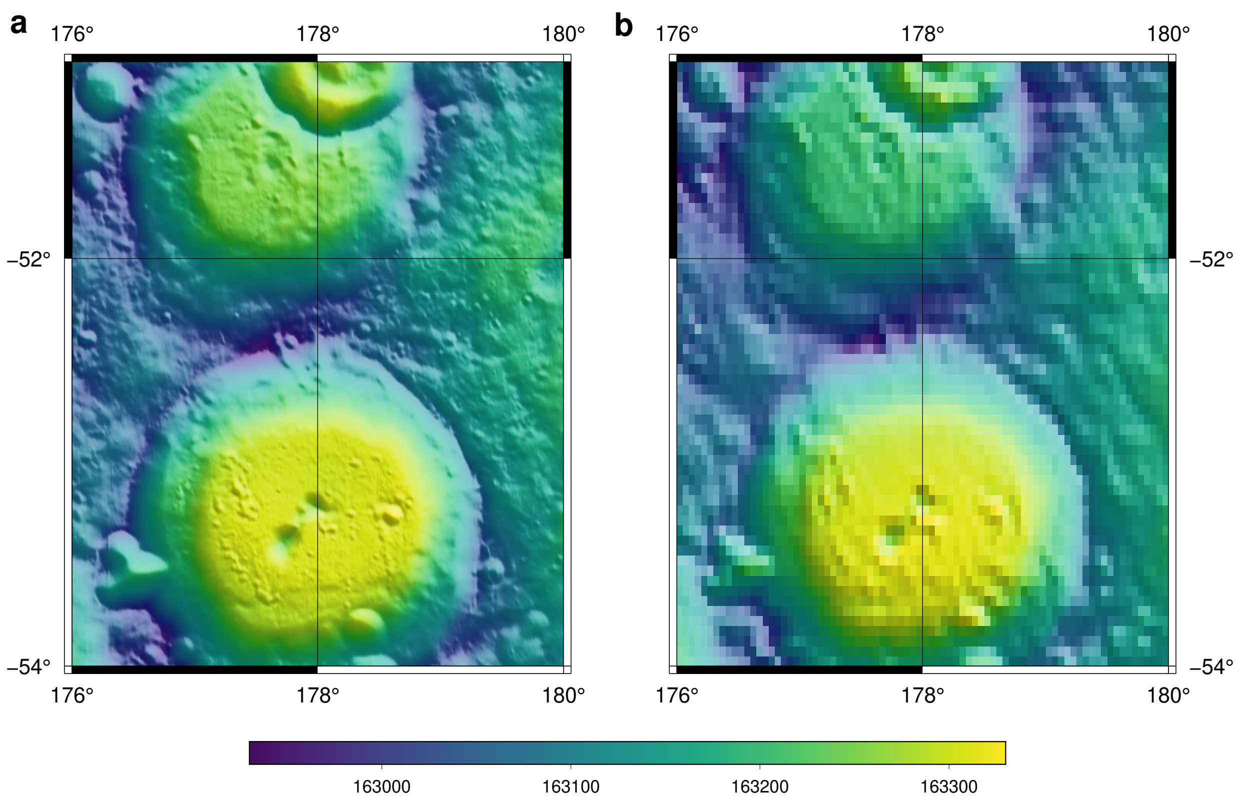

Figure 13: Gravitational acceleration in mGal from LGM2026 (a) and LGM2011 (b). Both models are shown in their full resolution. The centrifugal acceleration was removed from LGM2011. LGM2026 is shown in the Moon's principal axes coordinate system and LGM2011 is shown in the Mean-Earth/Polar-Axis coordinate system.

prospective landing sites, inertial navigation (Zemba et al., 2024), to verify/calibrate readings of accelerometers or to derive quantities such as gravity anomalies or deflections of the vertical. *The maps of the gravitational tensor* can be used for autonomous navigation of spacecraft based on gravity gradient measurements (Chen et al., 2023) or for upward/downward continuation of the gravitational potential and vector in mass-free space. *Maps on the circumscribing sphere* can be helpful for studying spectral properties of the lunar external gravitational field to ~250-m spatial scales or for combining with the surface maps to radially interpolate the lunar gravitational field. Considering that the synthesis of spherical-harmonic gravity models is a routine task, users can readily use *the residual gravitational maps* to supplement long wavelengths (harmonics up to degree 500) also from spherical-harmonic models other than GRGM1200B. *Spherical-harmonic coefficients of the gravitational potential to degree 11,519* can be useful for studying the lunar gravitational field at fine scales in the spectral domain, to study convergence/divergence of spherical harmonics at the lunar surface or to check/derive empirical power rules for the spectrum of the gravitational field of the Moon.

7. Limitations

Short-scale LGM2026 signals (beyond degree 500, wavelengths smaller than ∼11 km at the equator) do not rely on observed gravity but instead on gravity modeled from topography and density. Therefore, LGM2026 must not be geophysically or geologically interpreted at these scales.

Noise is present in the grids of the gravitational potential, the gravitational vector and the gravitational tensor on the circumscribing sphere at spatial scales smaller than ∼9 km (beyond degree 600), ∼2 km (beyond degree 2500) and ∼650 m (beyond degree 8500), respectively (see Section 3.5). This seems to be caused by the combination of the attenuated gravitational field and by the limited accuracy of our gravity-forward modeling in the spatial domain. The surface grids are not affected by this issue, because the short-scale gravitational signals are much stronger at the lunar surface (see Section 3.5).

LDEM128 errors such as spikes or stripes (see Section 5.1.2) propagated into LGM2026 through the vertical position of evaluation points and through RTM. Visual screening of LGM2026 suggests the artifacts are found mostly (but not only) in latitudes $|\varphi| > 60°$.

8. Conclusions

LGM2026 is a set of lunar gravitational maps showing the gravitational potential, the gravitational vector and the gravitational tensor at the lunar surface and on its circumscribing sphere at a spatial resolution of 128 PPD (∼250 m at the equator). The maps combine GRAIL gravity (wavelengths up to ∼11 km at the equator) with gravity obtained by forward modeling of the LRO and Kaguya topography and 3D crustal density (scales smaller than ∼11 km). Besides the gravitational maps, LGM2026 provides an external spherical-harmonic expansion of the lunar gravitational field up to degree 11,519. To avoid divergence of spherical harmonics, the series should only be evaluated above the minimum sphere completely encompassing the Moon. Otherwise, it should be truncated appropriately based on a prior analysis. The commission error of LGM2026 is estimated at 2 mGal at the lunar surface in terms of the gravitational vector. LGM2026 is freely available under the open CC BY 4.0 license.

This study can also be viewed as a proposal and validation of a methodology for high-resolution gravity field modeling near planetary surfaces using 3D density models. This task is challenging, because the numerically efficient spherical-harmonic methods are generally invalid at planetary surfaces due to the divergence issue. On the other hand, spatial-domain methods such as prisms or tesseroids are valid in the entire 3D space, but they require massive parallelization to employ them globally at high resolutions. Our approach modifies the spherical-harmonic method and combines it with existing spatial-domain methods to retain accuracy and efficiency even at planetary surfaces. Once 3D variable density models of the Earth's topographic masses become available (Sheng et al., 2023), this framework is applicable also to the Earth's gravitational field.

CRediT authorship contribution statement

Blažej Bucha: Conceptualization, Methodology, Software, Validation, Formal analysis, Investigation, Resources, Data Curation, Writing – Original Draft, Writing – Review and Editing, Visualization, Project administration, Funding acquisition.

Declaration of competing interest

The author declares that he has no known competing financial interests or personal relationships that could have appeared to influence the work reported in this paper.

Acknowledgements

Two anonymous reviewers are gratefully acknowledged for their comments to improve the manuscript. Funded by the EU NextGenerationEU through the Recovery and Resilience Plan for Slovakia under the project No. 09I03-03-V04-00273. Part of the research results was obtained using the computational resources procured in the national project National competence centre for high performance computing (project code: 311070AKF2) funded by European Regional Development Fund, EU Structural Funds Informatization of society, Operational Program Integrated Infrastructure. We thank the HPC centre at the Slovak University of Technology in Bratislava, which is a part of the Slovak Infrastructure of High Performance Computing (SIVVP project, ITMS code 26230120002, funded by the European region development funds, ERDF). The maps were produced using the Generic Mapping Tools (Wessel et al., 2019). The plots were prepared with the Python's Matplotlib module (Hunter, 2007).

Data availability

LGM2026 is available at https://doi.org/10.5281/zenodo.19365932.

References

Balmino, G., Vales, N., Bonvalot, S., Briais, A., 2012. Spherical harmonic modelling to ultra-high degree of Bouguer and isostatic anomalies. Journal of Geodesy 86, 499–520. doi:10.1007/s00190-011-0533-4.

Barker, M.K., Mazarico, E., Neumann, G.A., Zuber, M.T., Haruyama, J., Smith, D.E., 2016. A new lunar digital elevation model from the Lunar Orbiter Laser Altimeter and SELENE Terrain Camera. Icarus 273, 346–355. doi:10.1016/j.icarus.2015.07.039.

Barthelmes, F., 2013. Definition of functionals of the geopotential and their calculation from spherical harmonic models: Theory and formulas used by the calculation service of the International Centre for Global Earth Models (ICGEM), http://icgem.gfz-potsdam.de. Scientific Technical Report STR09/02. GFZ German Research Centre for Geosciences. Potsdam, Germany. doi:10.2312/GFZ.b103-0902-26.

Besserer, J., Nimmo, F., Wieczorek, M.A., Weber, R.C., Kiefer, W.S., McGovern, P.J., Andrews-Hanna, J.C., Smith, D.E., Zuber, M.T., 2014. GRAIL gravity constraints on the vertical and lateral density structure of the lunar crust. Geophysical Research Letters 41, 5771–5777. doi:10.1002/2014GL060240.

Bucha, B., 2025. Spectral gravity forward modelling of 3D variable densities using an arbitrary integration radius with application to lunar topographic masses. Journal of Geodesy 99, 31. doi:10.1007/s00190-025-01951-9.

Bucha, B., 2026. CHarm: C/Python library for spherical harmonic transforms in planetary geodesy. Earth Science Informatics 19, 29. doi:10.1007/s12145-026-02076-z.

Bucha, B., Hirt, C., Kuhn, M., 2019. Cap integration in spectral gravity forward modelling: near- and far-zone gravity effects via Molodensky's truncation coefficients. Journal of Geodesy 93, 65–83. doi:10.1007/s00190-018-1139-x.

Bucha, B., Kuhn, M., 2020. A numerical study on the integration radius separating convergent and divergent spherical harmonic series of topography-implied gravity. Journal of Geodesy 94, 112. doi:10.1007/s00190-020-01442-z.

Bucha, B., Sansò, F., 2021. Gravitational field modelling near irregularly shaped bodies using spherical harmonics: a case study for the asteroid (101955) Bennu. Journal of Geodesy 95, 56. doi:10.1007/s00190-021-01493-w.

Chen, P., Mao, X., Sun, X., Lai, Y., 2023. Autonomous navigation for lunar final approach based on gravity gradient measurements. Advances in Space Research 71, 1769–1783. doi:10.1016/j.asr.2022.09.056.

Chin, G., Brylow, S., Foote, M., Garvin, J., Kasper, J., Keller, J., Litvak, M., Mitrofanov, I., Paige, D., Raney, K., Robinson, M., Sanin, A., Smith, D., Spence, H., Spudis, P., Stern, S.A., Zuber, M., 2007. Lunar Reconnaissance Orbiter overview: the instrument suite and mission. Space Science Reviews 129, 391–419. doi:10.1007/s11214-007-9153-y.

Driscoll, J.R., Healy, D.M., 1994. Computing Fourier transforms and convolutions on the 2-sphere. Advances in Applied Mathematics 15, 202–250.

Ďuríčková, Z., Janák, J., 2016. RTM-based omission error corrections for global geopotential models: case study in Central Europe. Studia Geophysica et Geodaetica 60, 622–643. doi:10.1007/s11200-015-0598-2.

Fisher, E.A., Lucey, P.G., Lemelin, M., Greenhagen, B.T., Siegler, M.A., Mazarico, E., Aharonson, O., Williams, J.P., Hayne, P.O., Neumann, G.A., Paige, D.A., Smith, D.E., Zuber, M.T., 2017. Evidence for surface water ice in the lunar polar regions using reflectance measurements from the Lunar Orbiter Laser Altimeter and temperature measurements from the Diviner Lunar Radiometer experiment. Icarus 292, 74–85. doi:10.1016/j.icarus.2017.03.023.

Forsberg, R., Tscherning, C.C., 1981. The use of height data in gravity field approximation by collocation. Journal of Geophysical Research 86, 7843–7854. doi:10.1029/JB086iB09p07843.

Goossens, S., Matsumoto, K., Liu, Q., Kikuchi, F., Sato, K., Hanada, H., Ishihara, Y., Noda, H., Kawano, N., Namiki, N., Iwata, T., Lemoine, F.G., Rowlands, D.D., Harada, Y., Chen, M., 2011. Lunar gravity field determination using SELENE same-beam differential VLBI tracking data. Journal of Geodesy 85, 205–228. doi:10.1007/s00190-010-0430-2.

Goossens, S., Sabaka, T.J., Wieczorek, M.A., Neumann, G.A., Mazarico, E., Lemoine, F.G., Nicholas, J.B., Smith, D.E., Zuber, M.T., 2020. High-resolution gravity field models from GRAIL data and implications for models of the density structure of the Moon's crust. Journal of Geophysical Research: Planets 125, e2019JE006086. doi:10.1029/2019JE006086.

Goossens, S.J., Smith, D.E., Zuber, M.T., Head, J.W., 2025. Shallow crustal density in the lunar south polar region. The Planetary Science Journal 6, 191. doi:10.3847/PSJ/adf05f.

Górski, K.M., Bills, B.G., Konopliv, A.S., 2018. A high resolution Mars surface gravity grid. Planetary and Space Science 160, 84–106. doi:10.1016/j.pss.2018.03.015.

Grafarend, E.W., Engels, J., 1993. The gravitational field of topographic-isostatic masses and the hypothesis of mass condensation. Surveys in Geohpysics 140, 495–524. doi:10.1007/BF00690574.

Grombein, T., Seitz, K., Heck, B., 2017. On high-frequency topography-implied gravity signals for a height system unification using GOCE-based global geopotential models. Surveys in Geophysics 38, 443–477. doi:10.1007/s10712-016-9400-4.

Han, S.C., Schmerr, N., Neumann, G., Holmes, S., 2014. Global characteristics of porosity and density stratification within the lunar crust from GRAIL gravity and Lunar Orbiter Laser Altimeter topography data. Geophysical Research Letters 41, 1882–1889. doi:10.1002/2014GL059378.

Hirt, C., 2012. Efficient and accurate high-degree spherical harmonic synthesis of gravity field functionals at the Earth's surface using the gradient approach. Journal of Geodesy 86, 729–744. doi:10.1007/s00190-012-0550-y.

Hirt, C., Bucha, B., Yang, M., Kuhn, M., 2019a. A numerical study of residual terrain modelling (RTM) techniques and the harmonic correction using ultra-high-degree spectral gravity modelling. Journal of Geodesy 93, 1469–1486. doi:10.1007/s00190-019-01261-x.

Hirt, C., Claessens, S., Fecher, T., Kuhn, M., Pail, R., Rexer, M., 2013. New ultrahigh-resolution picture of Earth's gravity field. Geophysical Research Letters 40, 4279–4283. doi:10.1002/grl.50838.

Hirt, C., Claessens, S.J., Kuhn, M., Featherstone, W.E., 2012. Kilometer-resolution gravity field of Mars: MGM2011. Planetary and Space Science 67, 147–154. doi:10.1016/j.pss.2012.02.006.

Hirt, C., Featherstone, W.E., 2012. A 1.5 km-resolution gravity field model of the Moon. Earth and Planetary Science Letters 329–330, 22–30. doi:10.1016/j.epsl.2012.02.012.

Hirt, C., Kuhn, M., 2014. Band-limited topographic mass distribution generates full-spectrum gravity field: Gravity forward modeling in the spectral and spatial domains revisited. Journal of Geophysical Research: Solid Earth 119, 3646–3661. doi:10.1002/2013JB010900.

Hirt, C., Kuhn, M., 2017. Convergence and divergence in spherical harmonic series of the gravitational field generated by high-resolution planetary topography—A case study for the Moon. Journal of Geophysical Research: Planets 122, 1727–1746. doi:10.1002/2017JE005298.

Hirt, C., Kuhn, M., Claessens, S., Pail, R., Seitz, K., Gruber, T., 2014. Study of the Earth's short-scale gravity field using the ERTM2160 gravity model. Computers and Geosciences 73, 71–80. doi:10.1016/j.cageo.2014.09.001.

Hirt, C., Reußner, E., Rexer, M., Kuhn, M., 2016. Topographic gravity modeling for global Bouguer maps to degree 2160: Validation of spectral and spatial domain forward modeling techniques at the 10 microgal level. Journal of Geophysical Research: Solid Earth 121, 6846–6862. doi:10.1002/2016JB013249.

Hirt, C., Yang, M., Kuhn, M., Bucha, B., Kurzmann, A., Pail, R., 2019b. SRTM2gravity: an ultrahigh resolution global model of gravimetric terrain corrections. Geophysical Research Letters 46, 4618–4627. doi:10.1029/2019GL082521.

Hofmann-Wellenhof, B., Moritz, H., 2005. Physical Geodesy. Springer, Wien, New York.

Hu, X., Jekeli, C., 2015. A numerical comparison of spherical, spheroidal and ellipsoidal harmonic gravitational field models for small non-spherical bodies: examples for the Martian moons. Journal of Geodesy 89, 159–177. doi:10.1007/s00190-014-0769-x.

Hunter, J.D., 2007. Matplotlib: A 2D graphics environment. Computing in Science & Engineering 9, 90–95. 10.1109/MCSE.2007.55.

Ince, E.S., Abrykosov, O., Förste, C., Flechtner, F., 2020. Forward gravity modelling to augment high-resolution combined gravity field models. Surveys in Geophysics 41, 767–804. doi:10.1007/s10712-020-09590-9.

Jekeli, C., 2017. Spectral Methods in Geodesy and Geophysics. CRC Press.

Kato, M., Sasaki, S., Takizawa, Y., the Kaguya project team, 2010. The Kaguya mission overview. Space Science Reviews 154, 3–19. doi:10.1007/s11214-010-9678-3.

Li, F., Yan, J., Xu, L., Shuanggen, J., Rodriguez, J.A.P., Dohm, J.H., 2015. A 10 km-resolution synthetic Venus gravity field model based on topography. Icarus 247, 103–111. doi:10.1016/j.icarus.2014.09.052.

Lin, M., Denker, H., Müller, J., 2020. Gravity field modeling using tesseroids with variable density in the vertical direction. Surveys in Geophysics 41, 723–765. doi:10.1007/s10712-020-09585-6.

Martinec, Z., Einšpigel, D., 2018. SHAVEL: A program for the spherical harmonic analysis of a horizontal vector field sampled in an equiangular grid on a sphere. Computer Physics Communications 233, 206–214. doi:10.1016/j.cpc.2018.06.015.

McClanahan, T.P., Parsons, A.M., Livengood, T.A., Su, J.J., Chin, G., Hamara, D., Harshman, K., Starr, R.D., 2024. Evidence for widespread hydrogen sequestration within the Moon's south pole cold traps. The Planetary Science Journal 5, 217. doi:10.3847/PSJ/ad5b55.

Neumann, G.A., 2024. LOLA MOON_PA gridded dataset [Data set]. NASA Goddard Space Flight Center Planetary Geodesy Data Archive. doi:10.60903/LOLA_PA.

Pavlis, N.K., Holmes, S.A., Kenyon, S.C., Factor, J.K., 2012. The development and evaluation of the Earth Gravitational Model 2008 (EGM2008). Journal of Geophysical Research 117(B04406), 1–38. doi:10.1029/2011JB008916.

Pollack, H.N., 1973. Spherical harmonic representation of the gravitational potential of a point mass, a spherical cap and a spherical rectangle. Journal of Geophysical Research 78, 1760–1768. doi:10.1029/JB078i011p01760.

Rexer, M., 2017. Spectral solutions to the topographic potential in the context of high-resolution global gravity field modelling. Ph.D. thesis. Technische Universität München. München, Germany.

Rexer, M., Hirt, C., Bucha, B., Holmes, S., 2018. Solution to the spectral filter problem of residual terrain modelling (RTM). Journal of Geodesy 92, 675–690. doi:10.1007/s00190-017-1086-y.

Sabaka, T.J., Nicholas, J.B., Goossens, S., Lemoine, F.G., Mazarico, E., 2014. Error propagation for high-degree gravity models developed from the GRAIL mission. https://pds-geosciences.wustl.edu/grail/grail-l-lgrs-5-rdr-v1/grail_1001/extras/clones/clone_description.pdf, (accessed October 02, 2025).

Sansò, F., 2013. Harmonic Calculus and Global Gravity Models, in: Sansò, F., Sideris, M.G. (Eds.), Geoid Determination: Theory and Methods. Springer-Verlag, Berlin, Heidelberg, pp. 111–168.

Sansò, F., Sideris, M.G., 2013. Geoid Determination: Theory and Methods. Springer, Berlin, Heidelberg.

Sheng, M., Shaw, C., Kingdon, R., 2023. Towards UNB_TopoDens version 3.0: The first global 3D topographical density model. URL: https://doi.org/10.57757/IUGG23-3164. XXVIII General Assembly of the International Union of Geodesy and Geophysics (IUGG) (Berlin 2023).

Šprlák, M., Han, S.C., 2021. On the use of spherical harmonic series inside the minimum Brillouin sphere: theoretical review and evaluation by GRAIL and LOLA satellite data. Earth-Science Reviews 222, 103739. doi:10.1016/j.earscirev.2021.103739.

Šprlák, M., Han, S.C., Featherstone, W.E., 2018. Forward modelling of global gravity fields with 3D density structures and an application to the high-resolution (~2 km) gravity fields of the Moon. Journal of Geodesy 92, 847–862. doi:10.1007/s00190-017-1098-7.

Šprlák, M., Han, S.C., Featherstone, W.E., 2020. Crustal density and global gravitational field estimation of the Moon from GRAIL and LOLA satellite data. Planetary and Space Sciences 192, 105032. doi:10.1016/j.pss.2020.105032.

Takahashi, Y., Scheeres, D.J., 2014. Small body surface gravity fields via spherical harmonic expansions. Celestial Mechanics and Dynamical Astronomy 119, 169–206. doi:10.1007/s10569-014-9552-9.

Tenzer, R., Foroughi, I., Sjöberg, L.E., Bagherbandi, M., Hirt, C., Pitoňák, M., 2018. Definition of physical height systems for telluric planets and moons. Surveys in Geophysics 39, 313–335. doi:10.1007/s10712-017-9457-8.

Tiesinga, E., Mohr, P.J., Newell, D.B., Taylor, B.N., 2021. CODATA recommended values of the fundamental physical constants: 2018. Reviews of Modern Physics 93. doi:10.1103/RevModPhys.93.025010.

Torge, W., Müller, J., 2012. Geodesy. 4 ed., Walter de Gruyter, Berlin. doi:10.1515/9783110250008.

Tziavos, I.N., Sideris, M.G., 2013. Topographic Reductions in Gravity and Geoid Modelling, in: Sansò, F., Sideris, M.G. (Eds.), Geoid Determination: Theory and Methods. Springer-Verlag, Berlin, Heidelberg, pp. 337–400.

Way, D.W., 2013. Preliminary assessment of the Mars Science Laboratory entry, descent, and landing simulation, in: 2013 IEEE Aerospace Conference, IEEE, Big Sky, MT, USA. doi:10.1109/AERO.2013.6497404.

Wessel, P., Luis, J.F., Uieda, L., Scharroo, R., Wobbe, F., Smith, W.H.F., Tian, D., 2019. The Generic Mapping Tools Version 6. Geochemistry, Geophysics, Geosystems 20, 5556–5564. doi:10.1029/2019GC008515.

Wieczorek, M.A., 2015. Gravity and topography of the terrestrial planets, in: Schubert, G. (Ed.), Treatise on Geophysics. 2 ed.. Elsevier. chapter 10.5, pp. 153–193. doi:10.1016/B978-0-444-53802-4.00169-X.

Wieczorek, M.A., 2024. Spherical harmonic models of the shape of the Moon (principal axis coordinate system) [LDEM128] (1.0.0) [Data set]. doi:10.5281/zenodo.11533784.

Wieczorek, M.A., Neumann, G.A., Nimmo, F., Kiefer, W.S., Taylor, G.J., Melosh, H.J., Phillips, R.J., Solomon, S.C., Andrews-Hanna, J.C., Asmar, S.W., Konopliv, A.S., Lemoine, F.G., Smith, D.E., Watkins, M.M., Williams, J.G., Zuber, M.T., 2013. The crust of the Moon as seen by GRAIL. Science 339, 671–675. doi:10.1126/science.1231530.

Williams, J.G., Konopliv, A.S., Boggs, D.H., Park, R.S., Yuan, D.H., Lemoine, F.G., Goossens, S., Mazarico, E., Nimmo, F., Weber, R.C., Asmar, S.W., Melosh, H.J., Neumann, G.A., Phillips, R.J., Smith, D.E., Solomon, S.C., Watkins, M.M., Wieczorek, M.A., Andrews-Hanna, J.C., Head, J.W., Kiefer, W.S., Matsuyama, I., McGovern, P.J., Taylor, G.J., Zuber, M.T., 2014. Lunar interior properties from the GRAIL mission. Journal of Geophysical Research: Planets 119, 1546–1578. doi:10.1002/2013JE004559.

Zemba, M.J., Vaden, K.R., Reinhart, R., Gramling, C.J., Heckler, G.W., 2024. NASA's lunar communications and navigation architecture: human lunar return. https://ntrs.nasa.gov/citations/20230016359.

Zuber, M.T., Smith, D.E., Watkins, M.M., Asmar, S.W., Konopliv, A.S., Lemoine, F.G., Melosh, H.J., Neumann, G.A., Phillips, R.J., Solomon, S.C., Wieczorek, M.A., Williams, J.G., Goossens, S.J., Kruizinga, G., Mazarico, E., Park, R.S., Yuan, D.N., 2013. Gravity field of the Moon from the Gravity Recovery and Interior Laboratory (GRAIL) mission. Science 339, 668–671. doi:10.1126/science.1231507.